European Journal of Medicinal Chemistry 254 (2023) 115286

Contents lists available at ScienceDirect

European Journal of Medicinal Chemistry

journal homepage: www.elsevier.com/locate/ejmech

Research paper

Discovery of a spirocyclic 3-bromo-4,5-dihydroisoxazole covalent inhibitor of hGAPDH with antiproliferative activity against pancreatic cancer cells

Andrea Galbiati [a,1], Stefania Bova [b], Raffaella Pacchiana [c], Chiara Borsari [d,a], Marco Persico [e], Aureliano Zana [a,1], Stefano Bruno [f], Massimo Donadelli [c], Caterina Fattorusso [e], Paola Conti [a,*]

[a] Department of Pharmaceutical Sciences, University of Milan, Via Mangiagalli 25, 20133, Milano, Italy
[b] Department of Medicine and Surgery, University of Parma, 43125, Parma, Italy
[c] Department of Neurosciences, Biomedicine and Movement Sciences, Section of Biochemistry, University of Verona, 37134, Verona, Italy
[d] Department of Biomedicine, University of Basel, Mattenstrasse 28, 4058, Basel, Switzerland
[e] Department of Pharmacy, University of Naples "Federico II", Via D. Montesano 49, 80131, Napoli, Italy
[f] Food and Drug Department, University of Parma, 43124, Parma, Italy

ARTICLE INFO

Handling Editor: Dr. Z Liu

Keywords:
Covalent inhibitor
Glyceraldehyde-3-phosphate dehydrogenase
3-Bromo-4,5-dihydroisoxazole
Anti-cancer activity
Glycolysis

ABSTRACT

Glyceraldehyde-3-phosphate dehydrogenase (GAPDH), a key glycolytic enzyme, plays a crucial role in the energy metabolism of cancer cells and has been proposed as a valuable target for the development of anticancer agents. Among a series of 5-substituted 3-bromo-4,5-dihydroisoxazole (BDHI) derivatives, we identified the spirocyclic compound **11**, which is able to covalently inactivate recombinant human GAPDH (hGAPDH) with a faster reactivity than koningic acid, one of the most potent hGAPDH inhibitors known to date. Computational studies confirmed that conformational rigidification is crucial to stabilize the interaction of the inhibitor with the binding site, thus favoring the subsequent covalent bond formation. Investigation of intrinsic warhead reactivity at different pH disclosed the negligible reactivity of **11** with free thiols, highlighting its ability to selectively react with the activated cysteine of hGAPDH with respect to other sulfhydryl groups. Compound **11** strongly reduced cancer cell growth in four different pancreatic cancer cell lines and its antiproliferative activity correlated well with the intracellular inhibition of hGAPDH. Overall, our results qualify **11** as a potent hGAPDH covalent inhibitor with a moderate drug-like reactivity that could be further exploited to develop anticancer agents.

1. Introduction

The inhibition of human glyceraldehyde-3-phosphate dehydrogenase (hGAPDH, EC 1.2.1.12), a key enzyme of the glycolytic pathway [1], is recognized as a valuable strategy for anticancer therapy [2–4]. The rationale behind this approach lies in the well-known Warburg effect, i.e., the shift of cancer cell metabolism from aerobic respiration to fermentation [5,6]. Indeed, most cancer cells convert glucose into lactate even in the presence of oxygen, and their metabolism is described as 'aerobic glycolysis'. As tumor cells show an increased dependence on glycolysis to meet their energy needs, they are more sensitive to hGAPDH inhibition than normal cells. Although hGAPDH is a ubiquitous enzyme, the increased dependence on hGAPDH activity and its overexpression in cancer cells led to the identification of this enzyme as a promising molecular target for cancer treatment [7]. Besides its role in glycolysis, hGAPDH exhibits several non-enzymatic 'moonlighting' roles. For example, cytoplasmic hGAPDH regulates mRNA stability and ER-to-Golgi trafficking, whereas nuclear hGAPDH modulates autophagy [8], and gene expression [9–11]. Moonlighting hGAPDH has also an emerging role in tumorigenesis [9], and this discovery further boosted the interest in its inhibition as a strategy for cancer therapy.

GAPDH catalyzes the conversion of glyceraldehyde 3-phosphate (GAP) into 1,3-biphosphoglycerate (1,3-BPG) [1], with the concomitant reduction of nicotinamide adenine dinucleotide (NAD^+) to NADH.

Abbreviations: hGAPDH, human glyceraldehyde-3-phosphate dehydrogenase; GAP, glyceraldehyde 3-phosphate; 1,3-BPG, 1,3-biphosphoglycerate; NAD^+, nicotinamide adenine dinucleotide; *Pf*GAPDH, *Plasmodium falciparum* GAPDH; GSH, glutathione; DBF, dibromoformaldoxime; BDHI, 3-bromo-4,5-dihydroisoxazole; KA, koningic acid; PL, pentalenolactone; EDTA, Ethylenediaminetetraacetic acid; βME, β-mercaptoethanol; MC, Monte Carlo.

* Corresponding author.
E-mail address: paola.conti@unimi.it (P. Conti).
[1] Philochem AG, Libernstrasse 3, CH-8112 Otelfingen, Switzerland.

https://doi.org/10.1016/j.ejmech.2023.115286
Received 17 January 2023; Received in revised form 10 March 2023; Accepted 13 March 2023
Available online 6 April 2023

The catalytic mechanism involves the nucleophilic attack of the thiolate side chain of a cysteine residue – C152 in the human ortholog – to the electrophilic carbonyl group of glyceraldehyde-3-phosphate. C152 owes this reactivity to its low pK_a (~6) and the enhanced nucleophilicity associated with the proximity of a histidine residue (H179) [12]. These properties make C152 more prone to covalent modifications by electrophilic reactive groups, dubbed warheads, leading to the enzyme irreversible inhibition [13]. In addition, covalent modifications of the catalytic Cys side chain occur physiologically, with S-nitrosylation dictating its cellular compartmentalization and apoptosis [11,14].

Only a few covalent inhibitors targeting the catalytic Cys of GAPDH – mostly used as chemical tools – have been reported [13], but most of them are rather small and unselective covalent binders, such as monomethylfumarate [15] and bromopyruvate [16]. One of the most potent GAPDH inhibitors is koningic acid (KA), a natural sesquiterpene isolated from *Trichoderma koningii* (Fig. 1) [17]. KA displays several biological activities, ranging from antimicrobial activity against anaerobic bacteria, antiparasitic properties [18], and anticancer activity [19,20]. Its ability to covalently react with the active site Cys is due to a reactive epoxide in its structure. A similar behavior is shown by pentalenolactone (PL), isolated from cultures of *Streptomyces arenae*, another sesquiterpene lactone containing a reactive epoxide ring [21] (Fig. 1). Highly reactive warheads in covalent chemical tools and drugs can lead to off-target reactions with cellular nucleophiles such as thiols, including glutathione (GSH). To our knowledge, the intrinsic reactivity of GAPDH inhibitors with thiols has not been assessed for covalent molecules targeting GAPDH, hampering the safe exploitation of these molecules in preclinical and early clinical trials.

We previously developed a series of *Plasmodium falciparum* GAPDH (*Pf*GAPDH) inhibitors as antimalarial agents [22–24], which were characterized by a 3-bromo-4,5-dihydroisoxazole (BDHI) nucleus exhibiting a tunable electrophilic reactivity towards the catalytic Cys depending on its substituents. In addition, we demonstrated the irreversibility of the reaction between this novel warhead and the catalytic Cys and the ability of these compounds to selectively react with the active-site Cys residue, sparing the other GAPDH Cys residues [24]. Very recently, we demonstrated that BDHI compounds acting as hGAPDH inhibitors are able to alter cancer metabolic profile and decrease cancer cell growth, without affecting normal cells [7].

Herein, starting from the structure of two previously developed *Pf*GAPDH [24] and hGAPDH [7] inhibitors (compounds **1** and **2**, Fig. 2) bearing a 5-aryl-BDHI nucleus, we explored the effects of substituents on the BDHI core and prepared a variety of substituted analogs. We built up a Structure-Activity Relationship (SAR) study and disclosed the intrinsic reactivity of the BDHI-based warhead. Their potency towards hGAPDH was tested, and the irreversible mode of action was confirmed. The observed SAR was rationalized using molecular modelling studies. Evaluation of the antiproliferative activity against pancreatic cancer cell lines allowed us to pinpoint **11** as a novel hGAPDH inhibitor with potential application as an anticancer agent. Moreover, we revealed that the BDHI intrinsic reactivity resembles that of unsubstituted acrylamides, the warhead mostly used in covalent clinical candidates and drugs. Therefore, the moderately reactive BDHI core could be further exploited in irreversible chemical probes to fine-tune electrophilicity and off-target reactivity.

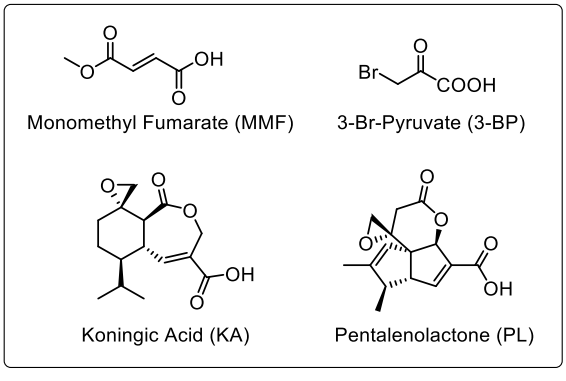

Fig. 1. Chemical structure of known GAPDH covalent inhibitors.

2. Results and discussion

2.1. Study design

The identification of **1** and **2** as hGAPDH inhibitors prompted us to explore the effect of the phenyl substituents on ligand potency. The hydroxyl group of **2** was replaced with a *p*-carboxylic acid (compound **3**), which is considered an important feature in GAPDH inhibitors since both KA and PL (Fig. 1) exhibit this acidic residue. Considering the increased potency of **3** (see Fig. 3), we investigated the effect of moving the carboxylic acid group in the *meta* (**4**) or *ortho* (**5**) position, and we replaced the *p*-carboxylic acid function with typical bioisosteric groups [25], including sulfonic acid (**6**), sulfonamide (**7**) and tetrazole (**8**). Afterwards, we focused on the phenyl/thiophene classical bioisosteric replacement [26] and generated compounds **9** and **10**. As an alternative strategy, inspired by the conformationally rigidified tri- and tetra-cyclic compounds KA and PL, we applied a rigidification approach, which is often exploited in drug design to minimize the entropic loss required for adopting a preferred conformation for binding. Rigidification is a powerful strategy for enhancing potency and selectivity for the pharmacological target [27]. The conformational restriction of a flexible ligand allowed us to explore a novel chemical space and generated the spirocyclic compounds **11** and **12** (Fig. 2).

2.2. Chemistry

The synthesis of the novel set of compounds (**3–12**) was performed starting from the appropriate vinyl derivative (Scheme 1), as previously reported for compounds **1** and **2** [24].

Alkene **22a** and **22d** were obtained from commercial sources, whereas **22b**, **c**, **e** were prepared by Wittig olefination of the corresponding aldehydes **21b**, **c**, **e** with triphenylphosphonium methyl bromide and potassium *tert*-butylate in dry THF (Scheme 1). All the aldehydes were commercially available. Alkenes **25**, **26**, **29**, and **30** were synthesized from the corresponding commercially available aldehydes (**23** and **24**) or ketones (**27** and **28**), following the same procedure described above. Alkene **22g** was obtained from commercially available 4-cyanostyrene **22f** by treating it with sodium azide and ammonium chloride in dry DMF at reflux. Afterwards, alkenes **22a-e**, **22g**, **25**, **26**, **29**, and **30** were submitted to 1,3-dipolar cycloaddition reaction with bromonitrile oxide, slowly generated *in situ* by dehydrohalogenation of dibromoformaldoxime (DBF), in an heterogeneous mixture of $NaHCO_3$ and ethyl acetate [28,29] to afford the desired 3-bromo-4,5-dihydroisoxazole (BDHI) derivatives **3–12**. All derivatives were obtained in their racemic form.

2.3. Inhibition of recombinant hGAPDH

In the search for novel hGAPDH inhibitors, compounds **1–12** were assessed as irreversible inhibitors of recombinant hGAPDH using a modified version of the Ferdinand assay [23], which consists in the detection of NADH production in the presence of GAPDH co-substrates GAP and arsenate, forming 1-arseno-3-phosphoglycerate. A preliminary screening was carried out for 3 h at a concentration of 100 μM (Fig. 3A), which allowed us to distinguish three different activity-based sub-classes. (i) Compounds **1–3**, **11**, and **12** produced an inhibition higher than 40%; (ii) **4**, **6**, and **10** between 20% and 40%; (iii) **5**, **7**, **8** and **9** were inactive. Among compounds **1**–**3**, the inhibitory activity increased going from the unsubstituted phenyl derivative **1**, through the

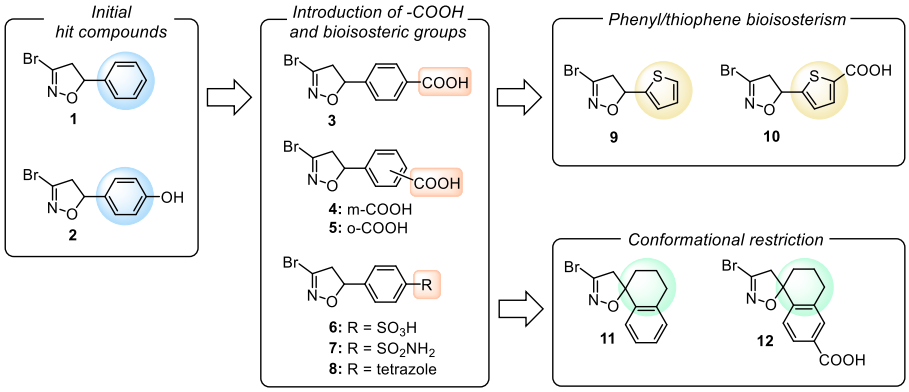

Fig. 2. Strategies for the development of novel hGAPDH inhibitors starting from the 3-bromo-4,5-dihydroisoxazole (BDHI) scaffold [7,24]: (i) introduction of carboxylic acid residue and bioisosteric groups, (ii) phenyl/thiophene bioisosteric replacement, and (iii) rigidification strategy.

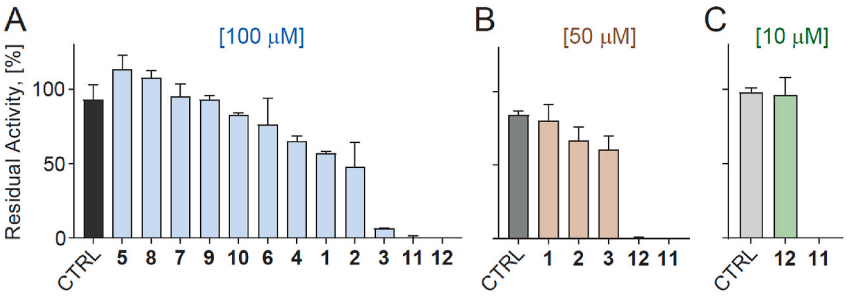

Fig. 3. (A, B, C) Residual activity (%) of hGAPDH upon incubation with (A) 100 μM of compounds **1–12** for 3 h; (B) 50 μM of compounds **1–3**, **11**, **12** for 30 min; (C) 10 μM of compounds **11** and **12** for 30 min. All experiments were performed at 25 °C in a buffered solution containing 10 mM TEA, 5 mM EDTA, 10 mM KH_2PO_4, pH 7.6. hGAPDH was at 2 μM concentration. CTRL: activity of hGAPDH maintained under the same conditions in the absence of inhibitors. Experiments were performed in independent duplicates. Data are shown as mean ± SD.

p-OH substituted derivative **2**, to compound **3** bearing a *p*-COOH. Moving the carboxylic group from the *para* to the *meta* (**4**) or *ortho* (**5**) position, a decrease in inhibitory activity was observed. The introduction in *para* position of carboxylic acid bioisosteres (**6–8**) characterized by different pK_a (Table S1), size, and shape (hybridization) led to a drop in activity, highlighting the *p*-COOH substitution as the most favorable for enzyme inhibition. These observations pointed out that the acidic nature of the *para* substituent was not the only factor affecting compound potency as its size and shape were crucial parameters too. The bioisosteric substitution of the benzene with a thiophene ring produced compounds with negligible inhibitory activity (**9** and **10**, Fig. 3A), although the presence of the –COOH substituent (**10**) slightly increased the activity. Finally, the conformational rigidification of **1** and **3** produced a remarkable effect on the inhibitory activity, with the spirocyclic compounds **11** (analogue of **1**) and **12** (analogue of **3**) able to fully inhibit hGAPDH activity at 100 μM concentration. The more active compounds (**1**–**3**, **11** and **12**, inhibition >40%) were selected for further investigation and tested at 50 μM for 30 min (Fig. 3B). hGAPDH was fully inhibited by compounds **11** and **12**. Interestingly, both molecules reacted much faster with the targeted enzyme than compounds **1** and **3**, their non-cyclized counterparts. Finally, we investigated **11** and **12** for 30 min at 10 μM, a 5-fold excess compared to the enzyme concentration (Fig. 3C). Under these conditions, which represent the resolution limit of our enzymatic assays, only compound **11** fully inhibited hGAPDH and was therefore selected for further studies. The spirocyclic compounds **11** and **12** showed a different SAR trend with respect to their acyclic counterparts, where the *p*-COOH substituted compound resulted in the most active, suggesting that the introduced structural rigidification induced a different binding mode.

For compound **11**, the time- and concentration-dependence typical of irreversible inhibitors [30] could not be characterized because of the limits of our enzymatic assay, which is based on minute-long enzyme kinetics that cannot be applied to compounds that inhibit GAPDH in comparable timeframes. Therefore, we monitored its reaction with hGAPDH by following the disappearance of the Racker band, a weak, broad absorption band ranging from 330 to 380 nm attributed to a charge transfer between the active site Cys and NAD^+ [24,31]. The Racker band is abolished by covalent modifications of the active site Cys, and is therefore indicative of covalent inhibition [32]. hGAPDH was incubated with **11,** its non-cyclized derivative (**1**), or KA, as a reference covalent inhibitor [17]. Compound **11** abolished the Racker band within 1 min (Fig. 4A). After 1 min, a weak residual band was observed in the presence of KA, whereas hGAPDH incubated with compound **1** still showed a residual band after more than 30 h (Fig. 4A). Therefore, we confirmed that compound **11** inhibits hGAPDH through the same mechanism observed for other 3-bromo-4,5-dihydroisoxazole (BDHI) derivatives [22–24], although the irreversible ligand-enzyme reactivity was significantly faster. To estimate the reaction rate, the disappearance of the Racker band was followed over time at 340 nm by incubating 100 μM of the enzyme with 200 μM of compounds **1**, **11** and KA (Fig. 4B). A high concentration of hGAPDH – and the correspondingly high concentration of inhibitors – was required due to the small extinction coefficient of the Racker band. Under our experimental conditions, the reaction kinetics of GAPDH with compound **11** analyzed with equation (1) exhibited a time constant (τ) of 0.2003 ± 0.009 min, 3.5-fold smaller than that observed for KA (0.701 ± 0.008 min). The reaction kinetics with GAPDH and compound **1** exhibited a τ of 908.2 ± 1.3 min, 4500-fold higher than compound **11**, its cyclized derivative, confirming the considerable positive impact of conformational rigidification on the biological activity.

2.4. Evaluation of intrinsic reactivity of 3-bromo-4,5-dihydroisoxazole (BDHI) derivatives

To rule out potential off-target toxicities, we assessed the intrinsic reactivity of selected BDHI derivatives with β-mercaptoethanol (βME). In addition, measurement of intrinsic warhead reactivity was essential to rationalize the SAR and test whether the significant increase in

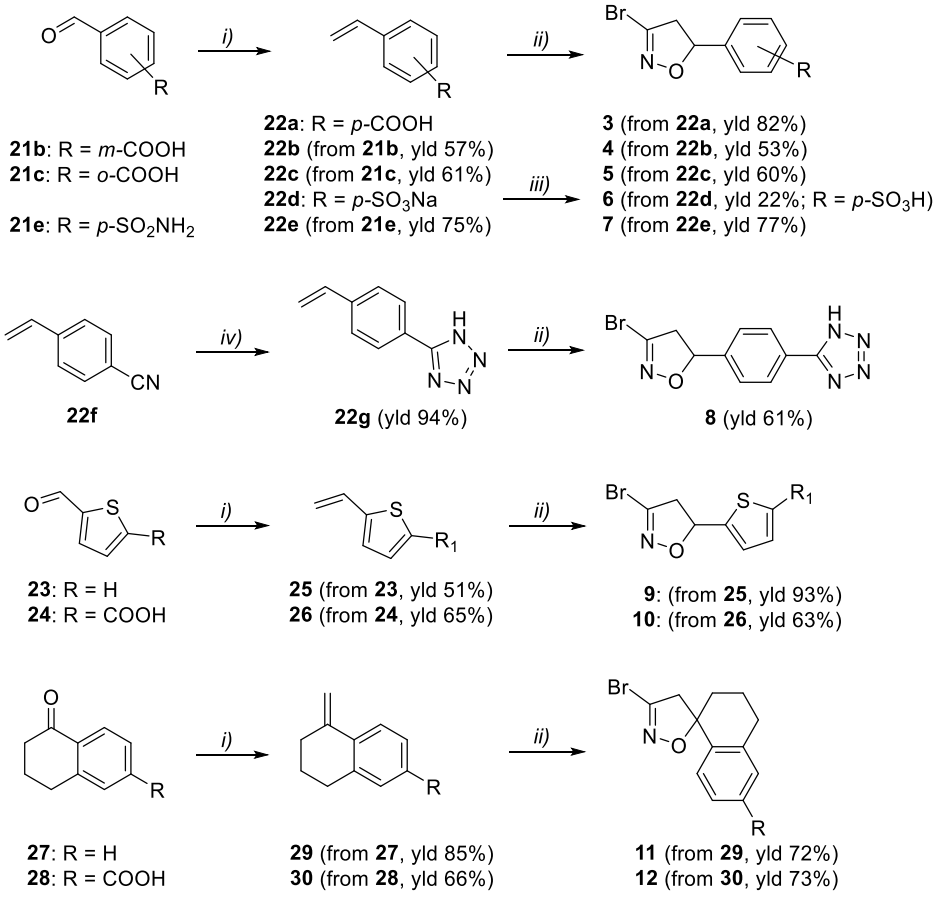

Scheme 1. Synthetic procedure for the preparation of compounds **3**–**12**[a].
[a]Reagents and conditions: (i) PPh_3CH_3Br, *t*BuOK, dry THF, rt; (ii) DBF, $NaHCO_3$, EtOAc, rt; (iii) (1) DBF, $NaHCO_3$, dioxane:H_2O (4:1), rt, (2) 2 N HCl; (iv) NaN_3, NH_4Cl, DMF, reflux.

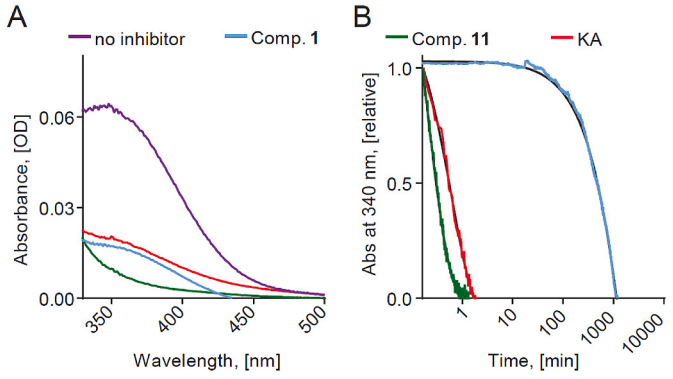

Fig. 4. (A) Absorption spectra and (B) kinetic traces at 340 nm of 100 μM hGAPDH before (purple line) and after incubation with 200 μM of compound **11** (green line), KA (red line), and compound **1** (light blue line) after 1 min (for compound **11** and KA) and 30 h (for compound **1**). The spectra were collected in a solution containing 10 mM TEA, 5 mM EDTA, 10 mM KH_2PO_4, pH 7.6. The traces were fitted with equation (1) (black lines, see Materials and Methods).

hGAPDH inhibitory activity observed upon rigidification was associated to an increased intrinsic reactivity towards thiol groups, or to improved interactions within hGAPDH active site.

The electrophilicity of the functional moiety responsible for the covalent bond formation plays a pivotal role in the development of irreversible chemical probes and drugs. In drug discovery programs, unsubstituted acrylamides are broadly exploited as warheads with minimal off-target reactions with unspecific nucleophiles inside cells (intracellular sulfhydryl concentration: 7 mM) [33]. The adduct formation with glutathione (GSH) or βME have been used as a surrogate for measuring the reactivity of cysteine-targeting warheads, and to determine the absolute rate constants (k_{chem}) for libraries of acrylamides [34]. Herein, we measured the rate constants of adduct formation of four selected BDHI derivatives (**1**, **3**, **11** and **12**, Fig. 5A). The compounds (1 mM) were incubated with an excess of βME (600 mM) in methanol/phosphate-buffered saline (PBS, pH 7.4) mixtures (v/v 4:1). Reaction progress and adduct formation (Fig. 5B) were monitored by LC-MS (see MS spectra in SI). The time-dependent curves of inhibitor consumption/adduct formation (Fig. 5C) were fitted using pseudo-first-order reaction kinetics (yielding k'), and used to calculate the second-order reaction rate constant (k_{chem}, Table 1), as previously described [34]. Considering the peculiar reactivity of the catalytic cysteine of GAPDH (pK_a6), we investigated the BDHI reactivity with βME (pK_a9) at different pH (7, 9 and 11). At pH 7, compound **1** showed an intrinsic reactivity comparable to unsubstituted acrylamides (Fig. 5C), matching the value of ibrutinib and a PI3Kα covalent inhibitor (see SI for chemical structure) within the same order of magnitude (k_{chem} **1**: $1.10{\cdot}10^{-4}$; ibrutinib: $10.4{\cdot}10^{-4}$; PI3Kαci: $3.70{\cdot}10^{-4}$ M^{-1} s^{-1}, Table 1). On the contrary, compounds **3** and **11** were poor electrophiles (k_{chem} **3**: $1.84{\cdot}10^{-6}$; **11**: $8.75{\cdot}10^{-6}$ M^{-1} s^{-1}), and **12** showed a negligible reactivity with 600 mM of βME at pH 7 ($k_{chem} \ll 1.00{\cdot}10^{-8}$, Fig. 5C and Table 1). The BDHI derivatives displayed improved reactivity at pH 9 (Fig. 5D and E), with **3** and **11** also reaching the intrinsic reactivity of the drug-like acrylamide-based warheads (k_{chem} **3**: $4.91{\cdot}10^{-4}$; **11**: $10.4{\cdot}10^{-4}$; PI3Kαci: $3.70{\cdot}10^{-4}$ M^{-1} s^{-1}, Table 1). In addition,

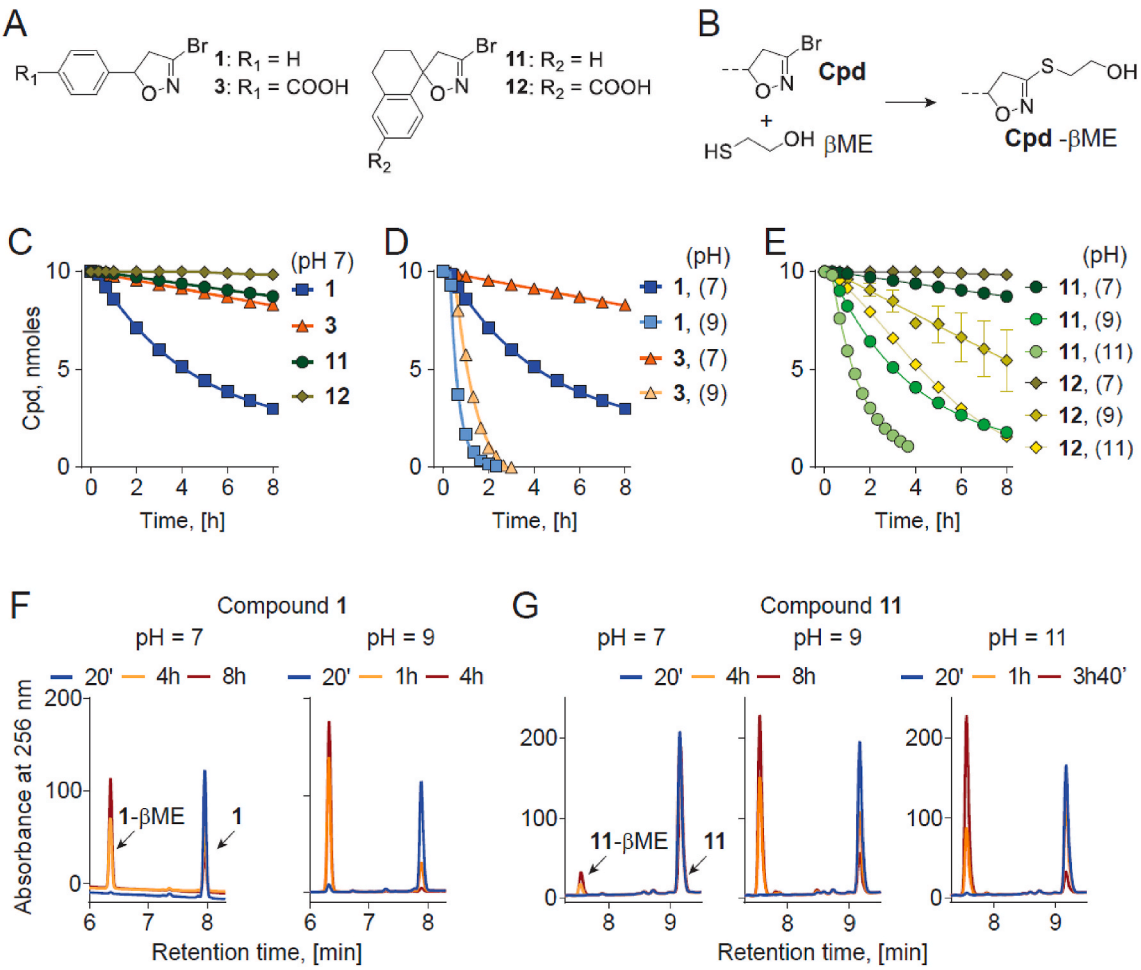

Fig. 5. (A) Chemical structure of a set of BDHI-containing compounds (**1**, **3**, **11** and **12**). (B) General reaction of warhead-containing compounds with βME. (C, D, E) Time-dependent inhibitor consumption curves used to calculate k_{chem}. Experiments were performed in independent duplicates. Data are shown as mean ± SD. Error bars not shown when smaller than symbols. The reaction has been investigated at different pH values: 7 (C, D, E), 9 (D, E) and 11 (E). (F, G) HPLC reaction monitoring of inhibitor (**1**, F; **11**, G) consumption and its βME adduct (**1-βME**, F; **11-βME**, G) formation.

Table 1
Reaction rate constants for four warhead-containing compounds (**1**, **3**, **11** and **12**) at different pH.

Comp.	pH	βME, [M]	k', [s^{-1}][a] mean ± SD		R^2	k_{chem}, [$M^{-1}•s^{-1}$][a] mean ± SD	
1[b]	7	0.6	$6.62·10^{-5}$	$0.28·10^{-5}$	0.9989	$1.10·10^{-4}$	$0.047·10^{-4}$
1	9	0.6	$7.52·10^{-4}$	$0.22·10^{-4}$	0.9991	$1.25·10^{-3}$	$0.037·10^{-3}$
3	7	0.6	$1.11·10^{-6}$	$<10^{-6}$	0.9969	$1.84·10^{-6}$	$<10^{-6}$
3	9	0.6	$2.95·10^{-4}$	$0.17·10^{-4}$	0.9980	$4.91·10^{-4}$	$0.29·10^{-4}$
11	7	0.6	$5.25·10^{-6}$	$<10^{-6}$	0.9994	$8.75·10^{-6}$	$<10^{-6}$
11	9	0.6	$7.61·10^{-5}$	$0.35·10^{-5}$	0.9985	$1.27·10^{-4}$	$0.058·10^{-4}$
11	11	0.6	$2.13·10^{-4}$	$0.026·10^{-4}$	0.9998	$3.55·10^{-4}$	$0.29·10^{-4}$
12	7	0.6	$\ll 1.00·10^{-8}$	–	–	$\ll 1.00·10^{-8}$	–
12	9	0.6	$2.45·10^{-6}$	$<10^{-6}$	0.8768	$4.08·10^{-6}$	$<10^{-6}$
12	11	0.6	$3.82·10^{-5}$	$1.03·10^{-5}$	0.9944	$6.37·10^{-5}$	$1.72·10^{-5}$
Ibrutinib[c]	7	0.6	–	–	–	$10.4·10^{-4}$	$0.32·10^{-4}$
PI3Kαci[c]	7	0.6	–	–	–	$3.70·10^{-4}$	$0.13·10^{-4}$

[a] Each mean and SD were calculated from two independent measurements. Compound concentration was always set at 1 mM.
[b] HPLC experiments performed without TFA.
[c] Acrylamide-based drug or chemical probe from Ref. [34].

compounds **11** and **12** were further investigated at pH 11 (Fig. 5E) were βME is entirely in the thiolate form. A pH-dependent increase of rate constants of adduct formation with βME was observed for all tested molecules (Fig. 5D–G). These results led to the identification of the BDHI core as a moderate reactive electrophile, which is expected to selectively bind to an activate cysteine with negligible reaction with cellular thiols.

2.5. Molecular modelling

The 3-bromo-4,5-dihydroisoxazole (BDHI) turned out to be an intrinsically moderate reactive warhead. Moreover, the differences observed in the intrinsic reactivity of compounds **1**, **3**, **11**, and **12** (Fig. 5) did not correlate with the inhibitory activity towards hGAPDH (Table 1). Comparing a potent (**11**) and a moderate (**1**) inhibitor of

hGAPDH, compound **11** showed an intrinsic reactivity of one order of magnitude weaker than compound **1**, highlighting that the increased efficiency in covalent bond formation was not related to an enhanced intrinsic reactivity. This suggested a remarkable proximity-driven covalent bond formation for compound **11**. To rationalize the observed SAR, we carried out computational studies to model the binding of **1** and **11** to hGAPDH catalytic site, and investigated how the introduced extra-volume and conformational restraint affected the binding and, therefore, the inhibitory activity.

Ligand analysis. The conformational space of the *R* and *S* enantiomers of compounds **1** and **11** was sampled by combining a stochastic conformational search procedure with DFT full optimization calculations, using the conductor-like polarizable continuum model (C-PCM) to mimic an aqueous environment [35] The BDHI derivatives **1** and **11** were characterized by a limited energetically accessible conformational space. In particular, within 5 kcal/mol from the global energy minimum, the **1** enantiomers showed just one orientation of the phenyl ring with respect to the BDHI ring, i.e., just one conformer, corresponding to a τ1 value of ~ −60° for the *R* enantiomer and ~60° for the *S* enantiomer (Table S2 and Fig. S1). In the case of **11**, each enantiomer presented two almost isoenergetic conformers (ΔE = 0.02 kcal/mol) sharing the same orientation of the phenyl ring found for **1**, while differing in the conformation of the bicyclic ring (τ3 = ± 60°; Table S3 and Fig. S2). The obtained conformers of the *R* and *S* enantiomers of **1** and **11** were used as starting ligand structures in the docking calculations.

Docking calculations. The aim of docking studies was to simulate the binding of our compounds to hGAPDH before the nucleophilic attack by the catalytic cysteine residue (C152). This latter could be approached from different binding sites also depending on the conformational/functional state of the enzyme [32,36–39]. According to the flip-flop model proposed for the reaction mechanism of GAPDH [32,36], the substrate initially binds by positioning the C-3 phosphate in the P_I site (Fig. 6A), afterwards, when the hydride ion is transferred to NAD^+, it rotates around the catalytic Cys moving the C-3 phosphate to a second site (P_{II} in Fig. 6A) and vacating the P_I site for the incoming inorganic phosphate (initially bound to another site, P_{III} in Fig. 6A) [37,38]. The

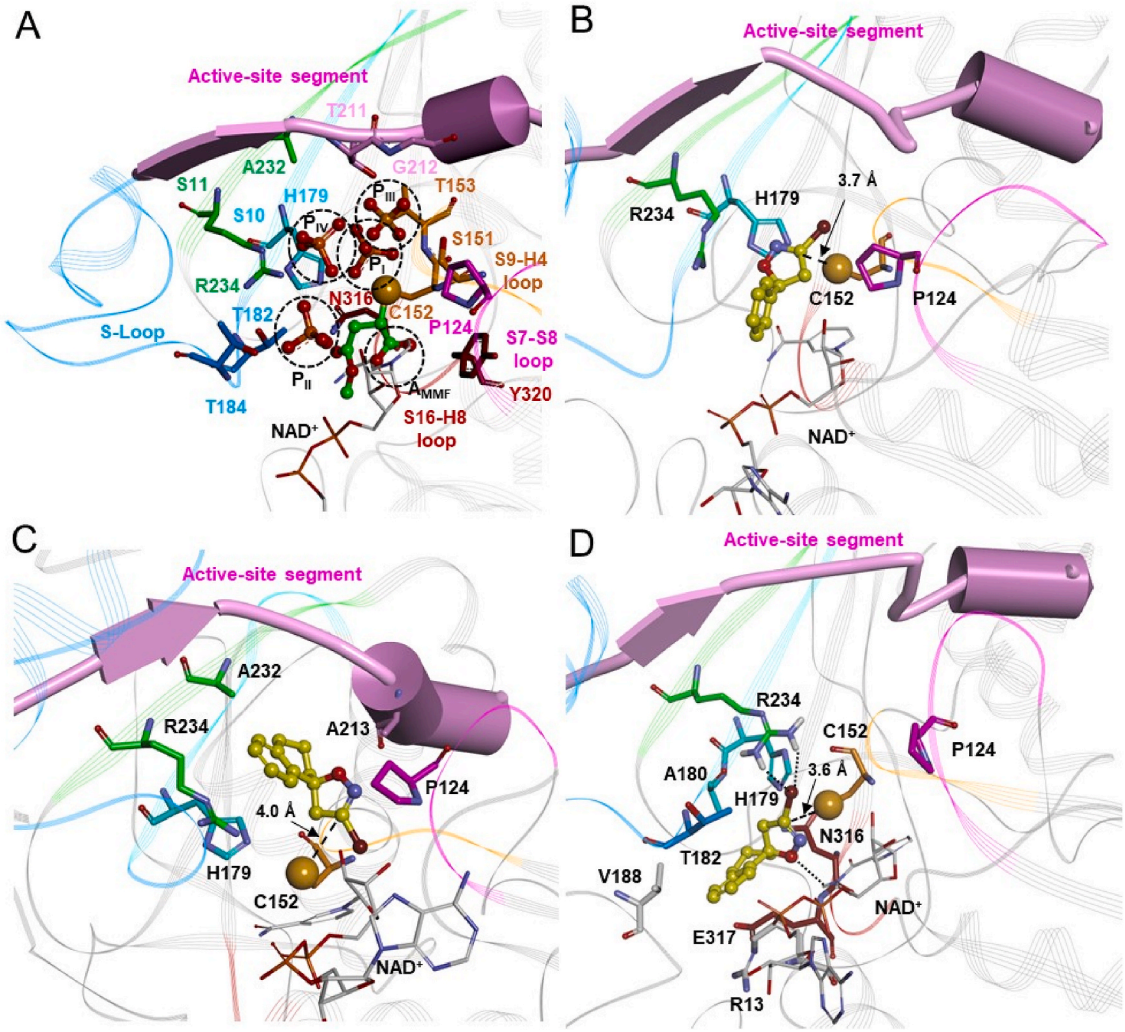

Fig. 6. (A) hGAPDH (PDB ID: 1ZNQ) active site substructures involved in the interaction with substrate, inhibitors, and anions. The key interaction residues are displayed and labelled. The binding sites P_I-P_{IV} and A_{MMF} are highlighted with black dashed circles. (B) Docked complex of (*S*)-**1**/hGAPDH. (C) Docked complex of (*S*)-**11**/hGAPDH. (D) Docked complex of (*R*)-**11**/hGAPDH. The structure of hGAPDH is displayed as line ribbon and colored in grey. The S7–S8 loop (aa122-129) is colored in magenta, the S9–H14 loop (aa149-153) in orange, the S10 strand (aa171-180) in cyan, the S-loop (aa181-207) in light blue, the S11 strand (aa228-235) in green, and the S16–H8 loop (aa315-320) in brown. The active-site segment (aa208-220) is displayed in cartoon form and colored in pink. Phosphate ions, monomethyl fumarate (MMF, carbon atoms colored in green) and ligands (carbon atoms colored in yellow) are displayed in ball&stick while the interacting residues and NAD^+ (carbon atoms colored in white) in stick. The sulfur atom of C152 is displayed in CPK (scaled by 50%). The distance between the electrophilic carbon C3 of BDHI ring and the C152 sulfur atom is showed (B–D). Hydrogen atoms are omitted for clarity, except those involved in hydrogen bond interactions (black dashed lines).

phosphate group of an analogue of the thioacyl reaction intermediate [39] as well as other negatively charged groups (PDB ID: 6GFP and 1S7C in Table S4), interact with a fourth anion binding site (P_{IV} in Fig. 6A) likely mimicking an intermediate position of the substrate when flipping from the P_I to the P_{II} site.

Accordingly, a Monte Carlo-based docking procedure was applied considering the whole protein and the ligand as flexible. Conformational restraints and filtering criteria (described in the experimental section) were rationally designed based on the data acquired by the analysis of the experimentally determined structures of GAPDH (apo form, holo form, and in complex with ligands or ions; Table S4) and used during the docking simulation. At the end of the docking procedure, to allow structure relaxation, the complexes were subjected to energy minimization calculations removing all the restraints (except the distance restraint between C152 and H179) and again checked using the filtering criteria.

For each ligand, the complex showing the most favorable interaction energy was selected as the best docked complex and its structural quality was assessed (Table S5). In all selected complexes the putative ligand bioactive conformation matched the structure of the GM conformer with a calculated RMSD value < 0.5 Å. (*S*)-**1** and (*R*)-**1** showed a less favorable binding energy with respect to (*S*)-**11** and (*R*)-**11** (Tables S6–S10), in line with their inhibitory potency against hGAPDH. Moreover, the enantiomers of **1** showed different binding modes with respect to those of **11** (Fig. 6B–D and Fig. S3), accounting for the different SAR trend of the spirocyclic compounds with respect to their acyclic counterparts.

In particular, it resulted that the *S* and *R* enantiomer of **1** are both able to approach the catalytic cysteine when positioning the phenyl ring at the P_{II} site (cation-π interaction with R234) and pointing the bromine atom towards the active-site segment (Fig. 6B; Fig. S3; Tables S6–S7). However, the BDHI ring is rotated about 180° in one enantiomer with respect to the other (Fig. 6B vs Fig. S3), and, after unrestrained energy minimization, (*R*)-**1** moved away (4.1 Å) from the catalytic residue C152 inducing a conformational change in the S7–S8 loop (Fig. S4).

On the other hand, each of the two enantiomers of **11** adopt a different binding mode, even though both of them presented a suitable orientation for the reaction with C152 (distance <4 Å [40,41], Fig. 6C–D). (*S*)-**11** placed the bicyclic ring between the P_I and P_{IV} sites, in a pocket delimited by the S10 strand (π-π interactions with H179), the active-site segment (hydrophobic interactions with A213), the S11 strand (hydrophobic interactions with A232 and cation-π interactions with R234), and the S7–S8 loop (hydrophobic interactions with P124), while the bromine atom pointed towards NAD^+ being attracted by the positive charge of the co-factor (Fig. 6C; Table S8). This binding mode supports the irreversible reaction involving the exit of bromine ion together with NAD^+ from the catalytic site of hGAPDH after the nucleophilic attack occurs (similarly to the GAP hydride ion during the catalytic reaction).

Notably, the calculated binding mode and interactions of (*S*)-**11** reproduces those of KA in the experimentally determined hGAPDH/KA complex (Fig. 7A; Table S8 vs Fig. S5).

In the case of (*R*)-**11**, it showed a suitable orientation for the reaction with C152 when positioning the bicyclic moiety in the pocket delimited by the S10 strand (A180), the S-loop (T182), and the S-loop of the adjacent subunit (V188) (Fig. 6D). The BDHI ring establishes π-π interactions with H179 (S10 strand) and the bromine atom points toward the P_I site forming a hydrogen bond with R234 (S11 strand) (Table S9). Since the conformational switch of R234 during the catalysis has been proposed to play an important role in the regulation of substrate flipping and product release [42], then it is conceivable that the bromine ion could promptly leave the catalytic site by taking advantage of this regulation mechanism.

The calculated binding mode of (*R*)-**11** to hGAPDH partially overlaps with one of the two experimentally determined binding sites of the acyl moiety of MMF (Fig. 7B). Indeed, after the nucleophilic attack by the catalytic Cys, the hybridization of MMF (C2 and C3 carbon atoms) changes from sp^2 to sp^3 and the inhibitor can adopt two binding modes (Fig. S6), still pointing the carboxylic group toward the S7–S8 loop (A_{MMF} site in Fig. 6A) [43]. In both cases, the covalent adduct of MMF with C152 overlaps with the NAD^+ binding site leading to the displacement of the co-factor [43]. Notably, the approach of (*R*)-**11** to the catalytic cysteine also induced an evident shift of NAD^+ with respect to its original position (RMSD: 4.3 Å; Fig. 6D).

The docking of (*S*)-**11** and (*R*)-**11** to hGAPDH induced significant conformational changes in i) the S7–S8 loop (aa122-129), ii) the active-site segment (aa208-220), and iii) the S-loop (aa181-207) (Fig. 6C–D vs A). The S7–S8 loop is involved in the binding of the co-factor (S122) and it was particularly affected by the binding of (*R*)-**11**, in agreement with

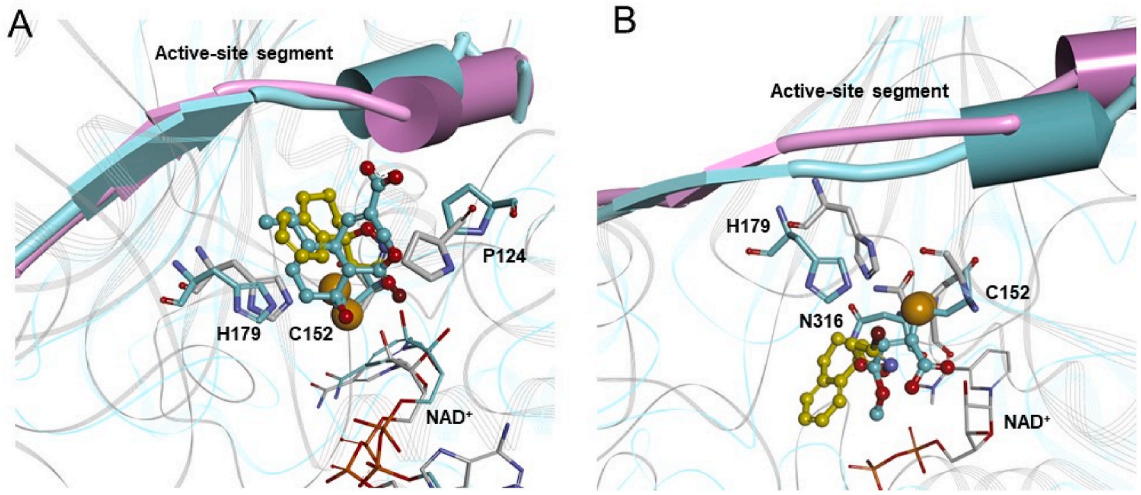

Fig. 7. Structural superimposition (Cα atoms) of: (A) the (*S*)-**11**/hGAPDH docked complex (ligand: ball&stick with carbon atoms colored in yellow; protein: line ribbon colored in grey and carbon atoms colored in white) on the X-ray structure of hGAPDH in complex with KA (KA: ball&stick with carbon atoms colored in cyan; protein: line ribbon and carbon atoms colored in cyan; PDB ID: 6M61); (B) the (*R*)-**11**/hGAPDH docked complex (ligand: ball&stick with carbon atoms colored in yellow; protein: line ribbons colored in grey and carbon atoms colored in white) on the X-ray structure of hGAPDH in complex with MMF (MMF: ball&stick with carbon atoms colored in cyan; protein: line ribbon and carbon atoms colored in cyan; PDB ID: 6IQ6). The interacting residues and NAD^+ (carbon atoms colored in white) are displayed in stick. The sulfur atom of C152 is displayed in CPK (scaled by 50%). Ligands, KA, MMF, NAD^+, and residues are colored by atom type (N = blue, O = red, S = yellow, P = orange, Br = brown). Hydrogen atoms are omitted for clarity.

the above mentioned shifting of NAD^+. On the other hand, in the hGAPDH/(*S*)-**11** complex, the S7–S8 loop moved close to the spirocyclic ligand due to a favorable interaction with P124 (Table S8), similarly to what observed for KA (Fig. S5), with which (*S*)-**11** shares a similar binding pocket/mode (Fig. 7A; Table S8 vs Fig. S5). The active-site segment is involved in the binding and the translocation of the substrate and the phosphate ion during the catalysis, assuming an "out" conformation when the phosphate group is located in the P_{III} or P_{IV} site or an "in" conformation when the phosphate is positioned in the P_I site (the ternary state of enzyme poised for catalysis) [44]. The two enantiomers of **11** both occupied the P_I site and, thus, induced the "in" conformation of the active segment. Remarkably, the binding of (*S*)-**11** induced an overall conformational change in the active-site segment of hGAPDH similar to that induced by KA (Fig. 7A). Finally, the S-loop is responsible for inter-subunit interactions [45], forming a long ridge that separates the NAD^+ binding cavities of adjacent subunits, and it was hypothesized that its sequence variation between human and other organisms is responsible for a different functional behavior [46]. Thus, the hypothesized binding modes could also account for compound **11** inhibition of hGAPDH through a cooperative inhibition mechanism similar to that observed for other BDHI derivatives against *Pf*GAPDH [22–24].

The detailed binding mode comparison of **11** and **1** allowed us to conclude that the introduced structural cyclization/rigidification induced different binding modes both with respect to the acyclic counterpart and between the two spirocyclic enantiomers. The reversible binding of compound **11** into hGADPH catalytic site was stabilized by the rigidified scaffold, which favors the positioning of the warhead in proximity to the catalytic cysteine. Our docking results are in accordance with the experimental data showing a significant and faster hGAPDH inhibition by **11** with respect to **1**, that is guided by warhead proximity to the targeted nucleophilic amino acid side chain rather than its intrinsic electrophilicity.

2.6. Antiproliferative activity in pancreatic cancer cells

GAPDH levels were found elevated in human pancreatic ductal adenocarcinoma (PDAC) compared to normal pancreas [7]. Furthermore, we previously demonstrated that the oncogenic and mutant isoforms of p53, which frequently occur in PDAC patients, stabilize GAPDH cytoplasmic localization preventing its nuclear translocation. These findings supported the enhanced glycolysis of PDAC cells, and the suppression of cancer cell death mechanisms mediated by nuclear GAPDH [47]. To investigate the effect of the most active hGAPDH inhibitors on PDAC cell growth, we treated PaCa-3, PaCa-44, PANC-1, and MIA PaCa-2 cell lines with compounds **11** or **12** at different concentrations (ranging from 1 μM to 100 μM, Fig. 8A-D). Compound **11** turned out to strongly reduce cancer cell growth in all tested cell lines, while **12** displayed a modest antiproliferative effect only in PaCa-44 cell line at the highest concentration (100 μM). These results qualify **11** as a novel molecule able to specifically inhibit GAPDH and efficiently penetrate PDAC cells, thus causing cancer cell growth inhibition. The significantly lower effect displayed by compound **12** compared to **11** might be related to the reduced cellular permeability due to the presence at physiological

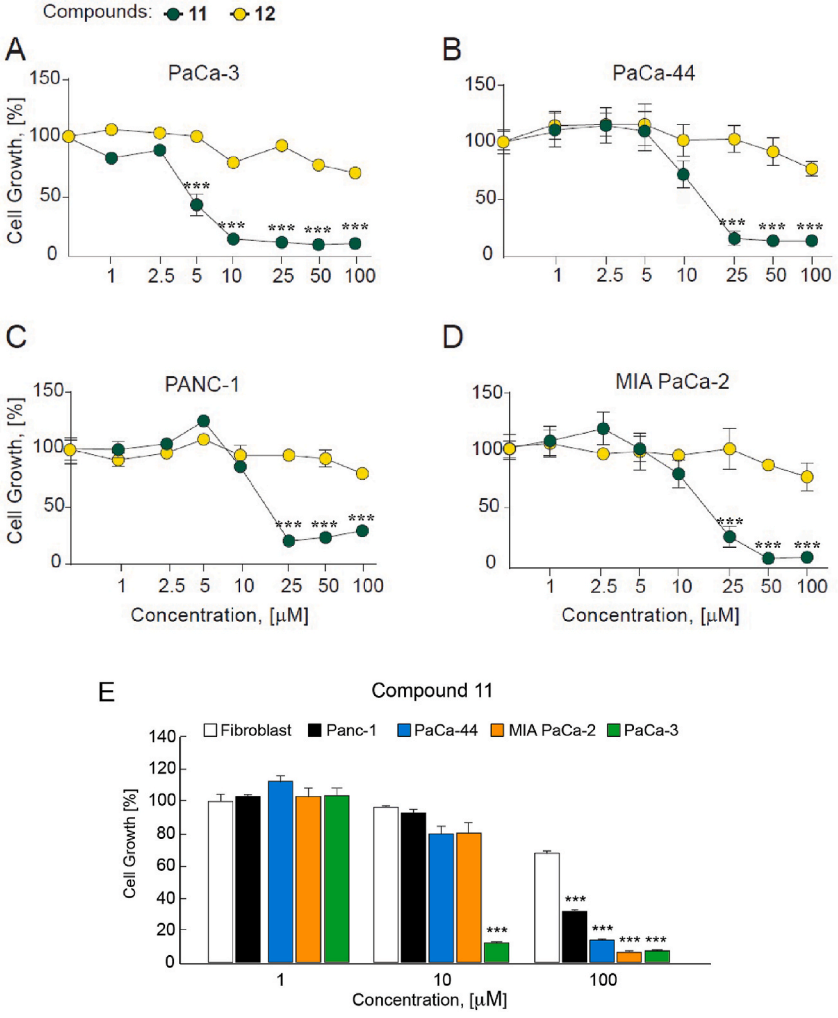

Fig. 8. (A–D) Cell growth after incubation with compounds **11** and **12**. Cells were treated with different concentrations (1 μM–100 μM) of two hGAPDH inhibitors for 48 h. DMSO control used as vehicle at the highest concentration tested did not affect cell growth on any cell line (data not shown). Cell growth was calculated using Crystal Violet assay and reported as a percentage compared to non-treated cells. The absorbance values of treated cell lines with each inhibitor were normalized on the absorbance values obtained on untreated cells. (E) Comparison between cell growth inhibition in PDAC cells and non-tumor cells (normal fibroblasts, white bar) for compound **11**. Results are shown as mean ± SD (n = 4). Statistical analysis was performed with multiple *t*-test comparing cell growth of treated *vs* untreated cells, ***$p < 0.0001$.

pH of a negatively charged carboxylate (**12** $cLogD_{7.4}$ = 0.96 vs **11** $cLogD_{7.4}$ = 4.42; Table S1), which can significantly reduce the intracellular concentration reached by the inhibitor. Indeed, at low concentrations (10 μM, see Fig. 3C), compound **12** was remarkably weaker than **11** in inhibiting hGAPDH.

Moreover, we investigated the cytotoxicity of **11** in non-tumor cells, treating normal fibroblasts with increasing concentrations of the tested compound. Interestingly, compound **11** determined a very slight antiproliferative effect on fibroblasts (~20%) even at the highest concentration (Fig. 8F), suggesting that its growth inhibition effect on PDAC cells may be strictly correlated with their cancerous nature and metabolism.

To further prove the anticancer potential of **11**, we investigated its antiproliferative effect in the four PDAC cell lines having differential *TP53* gene status. Interestingly, wild-type p53 cells (PaCa-3) were significantly more sensitive to compound **11** than PDAC cells carrying mutant *TP53* gene (Fig. 9). PaCa-3 cell growth percentage significantly decreased starting from 5 μM (42%), while other mutant p53 PDAC cell lines showed a moderate inhibitory effect only starting from 10 μM. The half-maximal inhibitor concentration (IC_{50}) values of compound **11** in wild-type p53 PaCa-3 cells was 3–4 times lower than those measured in mutant p53 PDAC cell lines (Table 2). These data are in line with previous observations of our lab and others, demonstrating the role of mutant isoforms of p53 in sustaining the glycolytic flux and promoting chemoresistance of PDAC cells [48,49]. Moreover, the enhanced sensitivity to GAPDH inhibition of cancer cells bearing wild-type p53 can also be explained by the fact that this tumor suppressor protein has an inhibitory role on the glycolytic flux [50], which may be additionally and excessively blocked by the treatment determining a metabolic default of cancer cells. However, as revealed by the curves in Fig. 8, high concentrations of compound **11** are able to inhibit cell growth also in PDAC cells bearing oncogenic mutant p53 isoforms.

2.7. Correlation between PDAC cell growth and GAPDH inhibition

To confirm that the antiproliferative activity observed in the different cell lines was associated with hGAPDH inhibition, we evaluated the inhibition of recombinant hGAPDH under similar conditions as those tested in the cell growth assays (48 h at 10 μM concentration, 37 °C). After 48 h, compound **11** produced full inhibition, whereas **12** produced only a 40% inhibition (Fig. 10). These results showed a good correlation with the growth experiments in PDAC cells (Fig. 8).

Aiming to further prove that the inhibition of PDAC cell lines was

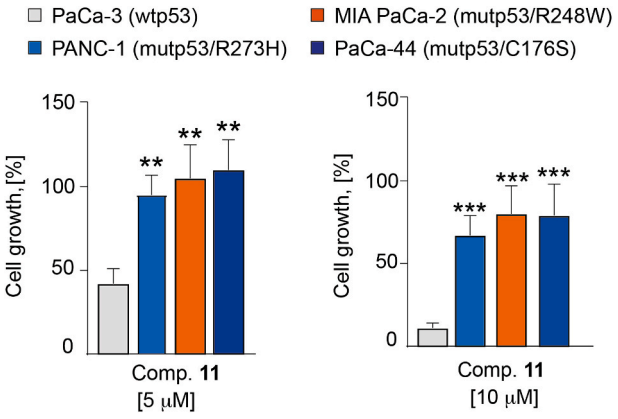

Fig. 9. Comparison between PaCa-3 (wtp53) and mutant p53 cell lines. After treatment with 5 μM and 10 μM of compound **11** for 48 h, cell growth was calculated using Crystal Violet assay and each cell line was normalized on its untreated control. Results are shown as mean ± SD (n = 4). Statistical analysis was performed with one-way ANOVA and Dunnet's multiple comparison tests between mutp53 *vs* wtp53 cell lines, $^{**}p < 0.05$, $^{***}p < 0.0001$.

Table 2
IC_{50} values of compound **11** in tested PDAC cell lines.

PDAC cell lines	Compound 11 IC_{50} ± SD (μM)
PaCa-3	4.69 ± 0.09
PaCa-44	16.16 ± 0.06
PANC-1	21.72 ± 0.04
MIA PaCa-2	15.20 ± 0.12

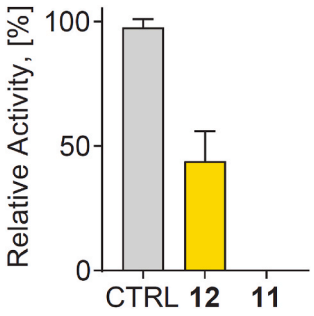

Fig. 10. Relative activity (%) of hGAPDH upon incubation with 10 μM of compounds **11** and **12** for 48 h at 37 °C in a buffered solution containing 10 mM TEA, 5 mM EDTA, 10 mM KH_2PO_4, pH 7.6. hGAPDH concentration: 2 μM. CTRL: non-treated hGAPDH activity. Experiments were performed in independent duplicates. Data are shown as mean ± SD.

associated with GAPDH irreversible inhibition, we measured GAPDH activity on lysates of Panc-1, PaCa-3 and PaCa-44 cells grown in the presence of either 10 or 100 μM of compounds **11** and **12**. Cells were flash-frozen, thawed, and resuspended in a solution containing 200 mM NaCl, 1 mM EDTA, 20 mM CHAPS, 10% sucrose. They were then subjected to three freeze-thaw cycles. The GAPDH activity of cell lysates was measured using the same assay described above, and the total protein content was measured using the Bradford assay. The ratio between the GAPDH activity and the total protein content was calculated and normalized to the ratio measured for the same cell line grown in the absence of inhibitors (Fig. 11). For all cell lines tested, compound **11** at 100 μM led to an undetectable GAPDH activity over the total protein content of the lysate, suggesting a full inhibition of the glycolytic pathway consistent with the observed cell mortality at the same concentration (Fig. 8). Full GAPDH inhibition was also observed at 10 μM, a concentration at which cell growth was only partially reduced (Fig. 8). Compound **12** led to an inhibition of intracellular GAPDH between 30 and 70%, with the highest inhibition observed for PANC-1 cells (Fig. 11).

The levels of inhibition of intracellular hGAPDH produced by **11** (Fig. 11) were consistent with those observed for recombinant hGAPDH under the same incubation conditions (Fig. 10), suggesting its ability to

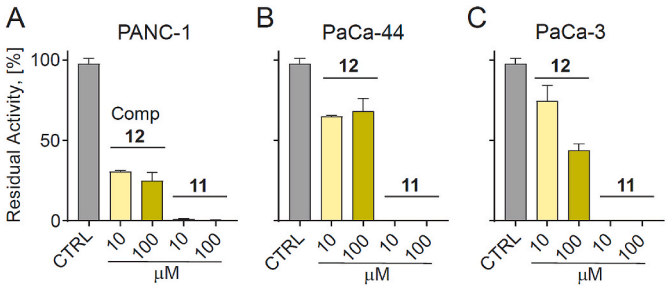

Fig. 11. Percent activity (%) of hGAPDH in cell lysates of PANC-1 (a), PaCa-44 (b), and PaCa-3 (c) upon incubation with either compounds **11** or **12** at 0 (CTRL), 10 or 100 μM concentration. The activity was normalized to the total protein content. Experiments were performed in independent duplicates. Data are shown as mean ± SD.

cross the cell membrane within the 48 h incubation time.

3. Conclusions

Targeting glycolysis is recognized as a promising strategy to develop anticancer agents. Herein, we disclosed a series of covalent inhibitors bearing the 3-bromo-4,5-dihydroisoxazole (BDHI) warhead and targeting the catalytic C152 of hGAPDH. Compound **11** was identified as a potent hGAPDH inhibitor, with higher potency than koningic acid, a well-known hGAPDH inhibitor. Computational studies confirmed that conformational rigidification was crucial to stabilize the interaction of the inhibitor within the binding site, thus favoring the covalent bond formation and leading to superior *in vitro* activity compared to the non-cyclized derivative **1**. Extensive investigation of the intrinsic reactivity of BDHI derivatives at different pH revealed the BDHI core to be a moderate reactive electrophile, which engages the desired target with negligible side reactions with cellular thiols. Compound **11** showed a reduced k_{chem} compared to that of **1**, highlighting that the improved efficacy in hGAPDH inhibition was driven by the optimal positioning of the warhead with respect to C152 rather than to an improved electrophilicity. We proposed a proximity-driven reactivity approach that allowed to increase the reaction rate constant of **11** with respect to **1** of 4.5×10^3-fold, while the electrophilicity of the warhead was decreased. The moderate reactive covalent inhibitors **11** and **12** were assessed in a panel of pancreatic cancer cell lines, and **11** showed a significant antiproliferative activity with a more marked effect against wild-type p53 cells. A good correlation between the antiproliferative activity and the ability to effectively inhibit intracellular hGAPDH was found. In this respect, physicochemical properties affecting membrane cell penetration also play a crucial role. The significantly lower antiproliferative activity of compound **12** is partly explained by a lower rate of penetration through the cancer cell membrane, accordingly to the lower $logD_{7.4}$ value.

The moderate intrinsic reactivity of **11**, its favorable physicochemical properties, the strong inhibition of hGAPDH, and the antiproliferative activity in cells are highly encouraging and suggest the exploitation of **11** as a chemical tool to deconvolute the interplay between glycolysis and cancer. In addition, **11** qualifies as a starting point for further optimization aimed at developing effective anticancer agents.

4. Material and methods

4.1. General experimental procedures

All reagents, solvents and starting materials **21b**, **21c**, **21e**, **22a**, **22d**, **22f**, **23**, **24**, **27** and **28** were purchased from Sigma-Aldrich, Fluorochem or TCI Europe. DBF was prepared according to literature [51]. ^{1}H NMR and ^{13}C NMR spectra were recorded with a Varian Mercury 300 (300 MHz) spectrometer. NMR spectra were obtained in deuterated solvents, such as $CDCl_3$, $(CD_3)_2SO$ or CD_3OD. The chemical shift (δ values) are reported in ppm and corrected to the signal of the deuterated solvents [7.26 ppm (^{1}H NMR) and 77.16 ppm (^{13}C NMR) for $CDCl_3$; 2.50 ppm (^{1}H NMR) and 39.52 ppm (^{13}C NMR) for $(CD_3)_2SO$; and 3.31 ppm (^{1}H NMR) and 49.00 ppm (^{13}C NMR) for CD_3OD]. Peak multiplicities are reported as: s (singlet), d (doublet), dd (doublet of doublets), ddd (doublet of doublet of doublets), dddd (doublet of doublet of doublet of doublets), t (triplet), dt (doublet of triplets), td (triplet of doublets), q (quartet), m (multiplet), br (broad). Chemical shifts (δ) are expressed in ppm and coupling constants (J) in Hertz (Hz). Thin layer chromatography (TLC) plates were purchased from Sigma-Aldrich (silica gel 60 F254 aluminum sheets, with fluorescence indicator 254 nm) and a dilute alkaline solution of $KMnO_4$ was used to visualize the compounds. Flash chromatography was performed using silica gel, pore size 60 Å, 230–400 mesh particle size. High-resolution mass spectra (HRMS) were performed with the SYNAPT G2-Si QTof High Definition Mass Spectrometer. Analyses were carried out either in positive or in negative ion mode. The chromatographic purity of final compounds was determined by LC-MS analyses performed on an Agilent 6100 Series Single Quadrupole MS system combined with a Agilent 1200 Series LC, using an InfinityLab Poroshell 120 EC-C18 Column (4.6 × 50 mm, 2.7 μm particle size, 120 Å pore size) at a flow rate of 0.8 mL/min, at room temperature, with linear gradients of solvents A and B (A = Millipore water with 0.1% HCOOH, B = ACN with 0.1% HCOOH) in 5 min. The purity of all final compounds was >95%. All hGAPDH inhibitors used for cell culture were solubilized in DMSO (100 mM) and stored at −80 °C until use. For *in vitro* assays using recombinant protein, the compounds were solubilized in DMSO at a concentration of 50 mM. Subsequent dilutions in DMSO were prepared as needed. DMSO alone was included as negative control in all experiments.

4.2. General procedures for the synthesis of the compounds

4.2.1. General procedure A

To a stirred suspension of methyltriphenylphosphonium bromide (3 eq) in dry THF (12 mL/mmol) under nitrogen atmosphere, tBuOK (3 eq) was added. The resulting yellow mixture was stirred for 30 min at room temperature. The mixture was cooled to 0 °C and a solution of aldehyde or ketone (1 eq) in dry THF (2 mL/mmol) was added dropwise. The reaction mixture was stirred overnight at room temperature, then quenched with a saturated aqueous solution of NH_4Cl and extracted with EtOAc. The resulting organic phases were collected, dried over anhydrous Na_2SO_4, filtered and evaporated under reduced pressure to afford a crude that was purified by flash chromatography.

4.2.2. General procedure B

To a stirred solution of alkene (1 eq) in EtOAc (4 mL/mmol), solid $NaHCO_3$ (5 eq) and 1,1-dibromoformaldoxime (1.5 eq) were added. The reaction mixture was stirred overnight at room temperature. Then, the reaction was diluted with water and extracted three times with EtOAc. The combined organic phases were collected, dried over Na_2SO_4, filtered and evaporated under reduced pressure to afford a crude that was purified by flash-chromatography or recrystallization.

4.2.3. General procedure C

To a stirred solution of alkene (1 eq) in EtOAc (4 mL/mmol), solid $NaHCO_3$ (5 eq) and 1,1-dibromoformaldoxime (1.5 eq) were added. The reaction mixture was stirred overnight at room temperature. Then, the reaction was diluted with water, acidified with 1 N HCl, and extracted three times with EtOAc. The combined organic phases were collected, dried over Na_2SO_4, filtered and evaporated under reduced pressure to afford a crude that was purified by flash-chromatography or recrystallization.

4.3. Synthesis of compounds

3-Vinylbenzoic acid (22b). Compound **22b** was prepared from 3-formylbenzoic acid (**21b**, 500 mg, 3.33 mmol) following general procedure A. Purification by flash chromatography (cyclohexane/EtOAc 9:1 + 1% AcOH) gave compound **22b** as a white solid (282 mg, 1.90 mmol, 57% yield). R_f = 0.50 (cyclohexane/EtOAc 8:2 + 0.5% AcOH); m. p. 95–97 °C; ^{1}H NMR (300 MHz, DMSO-d_6) δ 13.03 (br, 1H), 8.03–7.95 (m, 1H), 7.84 (ddd, J = 7.7, 1.7, 1.2 Hz, 1H), 7.73 (dddd, J = 7.8, 1.8, 1.2, 0.5 Hz, 1H), 7.47 (dd, J = 7.8, 7.7 Hz, 1H), 6.81 (dd, J = 17.7, 11.0 Hz, 1H), 5.90 (dd, J = 17.7, 0.8 Hz, 1H), 5.33 (dd, J = 11.0, 0.8 Hz, 1H); ^{13}C NMR (75 MHz, DMSO-d_6) δ 167.7 (s, 1C), 137.9 (s, 1C), 136.4 (s, 1C), 131.7 (s, 1C), 130.6 (s, 1C), 129.4 (s, 1C), 129.1 (s, 1C), 127.4 (s, 1C), 115.9 (s, 1C).

2-Vinylbenzoic acid (22c). Compound **22c** was prepared from 2-formylbenzoic acid (**21c**, 500 mg, 3.33 mmol) following general procedure A. Purification by flash chromatography (cyclohexane/EtOAc 9:1 + 1% AcOH) gave compound **22c** as a white solid (302 mg, 2.04 mmol, 61% yield). R_f = 0.42 (cyclohexane/EtOAc 8:2 + 0.5% AcOH); m.

p. = 97–99 °C; ^{1}H NMR (300 MHz, DMSO-d_6) δ 13.03 (br, 1H), 7.80 (ddd, J = 7.8, 1.5, 0.5 Hz, 1H), 7.71–7.62 (m, 1H), 7.57–7.49 (m, 1H), 7.42 (dd, J = 17.9, 11.0 Hz, 1H), 7.37 (dt, J = 7.5, 0.8 Hz, 1H), 5.73 (dd, J = 17.9, 1.4 Hz, 1H), 5.32 (dd, J = 11.0, 1.4 Hz, 1H); ^{13}C NMR (75 MHz, DMSO-d_6) δ 169.0 (s, 1C), 138.4 (s, 1C), 135.7 (s, 1C), 132.3 (s, 1C), 130.4 (s, 1C), 130.2 (s, 1C), 128.1 (s, 1C), 127.0 (s, 1C), 116.9 (s, 1C).

4-vinylbenzenesulfonamide (22e). Compound **22e** was prepared from 4-formylbenzenesulfonamide (**21e,** 500 mg, 2.70 mmol) following general procedure A. Purification by flash chromatography (cyclohexane/EtOAc 6:4) gave compound **22e** as a white solid (2.02 mmol, 370 mg, 75% yield). R_f = 0.42 (cyclohexane/EtOAc 1:1); m.p. 136–138 °C; ^{1}H NMR (300 MHz, Methanol-d_4) δ 7.93–7.72 (m, 2H), 7.67–7.53 (m, 2H), 6.81 (dd, J = 17.6, 11.0 Hz, 1H), 5.94 (dd, J = 17.6, 0.8 Hz, 1H), 5.40 (dd, J = 10.9, 0.8 Hz, 1H), two protons of –SO_2NH_2 not seen; ^{13}C NMR (75 MHz, Methanol-d_4) δ 142.4 (s, 1C), 141.3 (s, 1C), 135.4 (s, 1C), 126.3 (s, 2C), 126.1 (s, 2C), 116.0 (s, 1C).

5-(4-Vinylphenyl)-1*H*-tetrazole (22g). To a solution of 4-vinyl benzonitrile (**22f**, 200 mg, 1.55 mmol, 1 eq) in dry DMF (4 mL), NaN_3 (403 mg, 6.2 mmol, 4 eq) and NH_4Cl (298 mg, 5.58 mmol, 3.6 eq) were added. The reaction mixture was refluxed overnight. Solvent was evaporated under reduced pressure and the reaction mixture was acidified with 1 N aq. HCl and extracted with EtOAc (3 × 15 mL). The combined organic phases were washed with brine (20 mL), dried over anhydrous Na_2SO_4, filtered and evaporated under reduced pressure to give compound **22g** as a yellow solid (250 mg, 1.45 mmol, 94% yield). R_f = 0.72 (CH_2Cl_2/methanol 9:1); ^{1}H NMR (300 MHz, DMSO-d_6) δ 8.07–7.98 (m, 2H), 7.77–7.67 (m, 2H), 6.81 (dd, J = 17.7, 11.0 Hz, 1H), 5.99 (dd, J = 17.7, 0.9 Hz, 1H), 5.40 (dd, J = 11.0, 0.9 Hz, 1H), proton of tetrazole not seen; ^{13}C NMR (75 MHz, DMSO-d_6) δ 155.5 (s, 1C), 140.3 (s, 1C), 136.2 (s, 1C), 130.8 (s, 1C), 127.7 (s, 2C), 127.5 (s, 2C), 117.0 (s, 1C).

2-Vinylthiophene (25). Compound **25** was prepared from thiophene-2-carbaldehyde (**23**, 500 mg, 4.46 mmol) following general procedure A. Purification by flash chromatography (cyclohexane/EtOAc 99:1) gave compound **25** as a yellow oil (252 mg, 2.29 mmol, 51% yield). R_f = 0.49 (100% cyclohexane); ^{1}H NMR (300 MHz, $CDCl_3$) δ 7.19–7.14 (m, 1H), 7.04–6.92 (m, 2H), 6.80 (dd, J = 17.4, 10.9 Hz 1H), 5.57 (d, J = 17.4 Hz, 1H), 5.14 (d, J = 10.9 Hz, 1H); ^{13}C NMR (75 MHz, $CDCl_3$) δ 142.8 (s, 1C), 129.7 (s, 1C), 127.1 (s, 1C), 125.6 (s, 1C), 124.1 (s, 1C), 113.1 (s, 1C).

5-Vinylthiophene-2-carboxylic acid (26). Compound **26** was prepared from 5-formylthiophene-2-carboxylic acid (**24**, 500 mg, 3.20 mmol) following general procedure A. Purification by flash chromatography (cyclohexane/EtOAc 9:1 + 1% AcOH) gave compound **26** as a white solid (320 mg, 2.08 mmol, 65% yield). R_f = 0.38 (cyclohexane/EtOAc 8:2 + 0.5% AcOH); m.p. = 98–100 °C; ^{1}H NMR (300 MHz, Methanol-d_4) δ 7.63 (d, J = 3.8 Hz, 1H), 7.05 (d, J = 3.8 Hz, 1H), 6.86 (ddd, J = 17.4, 10.9, 0.6 Hz, 1H), 5.73 (d, J = 17.4 Hz, 1H), 5.29 (d, J = 10.9 Hz, 1H), proton of –COOH not seen; ^{13}C NMR (75 MHz, Methanol-d_4) δ 163.8 (s, 1C), 149.4 (s, 1C), 133.6 (s, 1C), 132.4 (s, 1C), 129.5 (s, 1C), 126.1 (s, 1C), 115.2 (s, 1C).

1-Methylene-1,2,3,4-tetrahydronaphthalene (29). Compound **29** was prepared from 3,4-dihydronaphthalen-1(2*H*)-one (**27**, 500 mg, 3.42 mmol) following general procedure A. Purification by flash chromatography (cyclohexane/EtOAc 99:1) gave compound **29** as a colorless oil (420 mg, 2.91 mmol, 85% yield). ^{1}H NMR (300 MHz, $CDCl_3$) δ 7.67–7.63 (m, 1H), 7.22–7.13 (m, 2H), 7.13–7.08 (m, 1H), 5.48 (d, J = 1.4 Hz, 1H), 4.96 (d, J = 1.5 Hz, 1H), 2.86 (t, J = 6.3 Hz, 2H), 2.55–2.52 (m, 2H), 1.90–1.84 (m, 2H); ^{13}C NMR (75 MHz, $CDCl_3$) δ 136.3 (s, 1C), 135.8 (s, 1C), 132.2 (s, 1C), 127.3 (s, 1C), 126.6 (s, 1C), 126.3 (s, 1C), 125.4 (s, 1C), 122.7 (s, 1C), 28.3 (s, 1C), 23.2 (s, 1C), 19.3 (s, 1C). The analytical data were in agreement with those reported in the literature [52].

5-Methylene-5,6,7,8-tetrahydronaphthalene-2-carboxylic acid (30). Compound **30** was prepared from 5-oxo-5,6,7,8-tetrahydronaphthalene-2-carboxylic acid (**28**, 500 mg, 2.63 mmol) following general procedure A. Purification by flash chromatography (cyclohexane/EtOAc 9:1 + 1% AcOH) gave compound **30** as a white solid (327 mg, 1.74 mmol, 66% yield). R_f = 0.54 (cyclohexane/EtOAc 8:2 + 0.5% AcOH); m.p. 166–167 °C; ^{1}H NMR (300 MHz, Methanol-d_4) δ 7.85–7.68 (m, 3H); 5.63 (q, J = 1.2 Hz, 1H); 5.08 (q, J = 1.4 Hz, 1H); 2.89 (t, J = 3.6 Hz, 2H); 2.63–2.52 (m, 2H); 1.95–1.81 (m, 2H); ^{13}C NMR (75 MHz, Methanol-d_4) δ 168.5, 142.9, 138.9, 137.1, 130.3, 129.1, 126.7, 123.9, 109.5, 32.6, 30.0, 23.4.

4-(3-Bromo-4,5-dihydroisoxazol-5-yl)benzoic acid (3). Compound **3** was prepared from 4-vinylbenzoic acid (**22a**, 200 mg, 1.35 mmol) following general procedure C. The crude solid product was triturated with dichloromethane and filtered under vacuum to give the compound **3** as a white solid (300 mg, 1,11 mmol, 82% yield). R_f = 0.30 (cyclohexane/EtOAc 7:3 + 0.5% AcOH); ^{1}H NMR (300 MHz, DMSO-d_6) δ 13.03 (br, 1H), 7.96 (d, J = 8.4 Hz, 2H), 7.49 (d, J = 8.1 Hz, 2H), 5.80 (dd, J = 10.9, 8.9 Hz, 1H), 3.82 (dd, J = 17.6, 11.0 Hz, 1H), 3.31 (dd, J = 17.6, 8.9 Hz, 2H); ^{13}C NMR (75 MHz, DMSO-d_6) δ 167.4 (s, 1C), 144.7 (s, 1C), 138.7 (s, 1C), 131.3 (s, 1 C), 130.2 (s, 2C), 126.9 (s, 2C), 82.5 (s, 1C), 48.5 (s, 1C). HPLC: t_r = 1.79 min, purity >95%. HRMS calcd for $C_{10}H_7^{79}BrNO_3$ [M − H]$^-$ 267.9609, found 267.9610. Calcd for $C_{10}H_7^{81}BrNO_3$ [M − H]$^-$ 269.9589, found 269.9588.

3-(3-Bromo-4,5-dihydroisoxazol-5-yl)benzoic acid (4). Compound **4** was prepared from 3-vinylbenzoic acid (**22b**, 200 mg, 1.35 mmol) following general procedure C. Recrystallization from ethyl acetate/*n*-hexane gave compound **4** as a white solid (192 mg, 0.71 mmol, 53% yield). R_f = 0.30 (cyclohexane/EtOAc 7:3 + 0.5% AcOH); m.p. = 135–138 °C; ^{1}H NMR (300 MHz, DMSO-d_6) δ 13.07 (br, 1H), 7.98–7.86 (m, 2H), 7.62 (dt, J = 7.8, 1.6 Hz, 1H), 7.54 (t, J = 7.9 Hz, 1H), 5.81 (dd, J = 10.9, 8.9 Hz, 1H), 3.81 (dd, J = 17.6, 10.9 Hz, 1H), 3.32 (dd, J = 17.6, 9.0 Hz, 1H); ^{13}C NMR (75 MHz, DMSO-d_6) δ 167.4 (s, 1C), 140.5 (s, 1C), 138.7 (s, 1C), 131.7 (s, 1C), 131.2 (s, 1C), 129.8 (s, 1C), 129.6 (s, 1C), 127.6 (s, 1C), 82.6 (s, 1C), 48.5 (s, 1C). HPLC: t_r = 1.82 min, purity >95%. HRMS calcd for $C_{10}H_7^{79}BrNO_3$ [M − H]$^-$ 267.9609, found 267.9607. Calcd for $C_{10}H_7^{81}BrNO_3$ [M − H]$^-$ 269.9589, found 269.9586.

2-(3-Bromo-4,5-dihydroisoxazol-5-yl)benzoic acid (5). Compound **5** was prepared from 2-vinylbenzoic acid (**22c**, 200 mg, 1.35 mmol) following general procedure C. The crude solid product was triturated with dichloromethane and filtered under vacuum to give compound **5** as a white solid (219 mg, 0.81 mmol, 60% yield). R_f = 0.40 (cyclohexane/EtOAc 8:2 + 0.5% AcOH); m.p. = 168 °C (dec.); ^{1}H NMR (300 MHz, DMSO-d_6) δ 13.21 (br, 1H), 7.94 (ddd, J = 7.7, 1.4, 0.5 Hz, 1H), 7.63 (dd, J = 1.3, 8.1 Hz 1H), 7.51 (dt, J = 0.6, 7.9 Hz, 1H), 7.45 (td, J = 7.5, 1.4 Hz, 1H), 6.32 (dd, J = 11.1, 7.3 Hz, 1H), 3.92 (dd, J = 17.8, 11.1 Hz, 1H), 3.08 (dd, J = 17.8, 7.3 Hz, 2H); ^{13}C NMR (75 MHz, DMSO-d_6) δ 168.2 (s, 1C), 142.3 (s, 1C), 138.6 (s, 1C), 133.1 (s, 1C), 131.3 (s, 1C), 128.7 (s, 1C), 128.5 (s, 1C), 126.0 (s, 1C), 80.9 (s, 1C), 49.9 (s, 1C). HPLC: t_r = 2.36 min, purity >95%. HRMS calcd for $C_{10}H_7^{79}BrNO_3$ [M − H]$^-$ 267.9609, found 267.9607. Calcd for $C_{10}H_7^{81}BrNO_3$ [M − H]$^-$ 269.9589, found 269.9586.

4-(3-Bromo-4,5-dihydroisoxazol-5-yl)benzenesulfonic acid (6). To a stirred solution of 4-styrenesulfonic acid sodium salt hydrate (**22d**, 200 mg, 0.89 mmol) in dioxane/water 4:1 (5 ml) were added solid $NaHCO_3$ (374 mg, 4.45 mmol, 5 eq) and 1,1-dibromoformaldoxime (270 mg, 1.33 mmol, 1.5 eq). The reaction mixture was stirred overnight at room temperature. Then, the reaction was diluted with water (5 mL) and extracted with EtOAc (5 mL). The aqueous phase was acidified with 1 N HCl, and extracted three times with EtOAc and the combined organic phases were collected, dried over Na_2SO_4, filtered and evaporated under reduced pressure. The crude was recrystallized from isopropanol to give compound **6** as a white solid (60 mg, 0.20 mmol, 22% yield). R_f = 0.20 (cyclohexane/EtOAc 7:3 + 0.5% AcOH); m.p. 250 °C dec. ^{1}H NMR (300 MHz, DMSO-d_6) δ 7.66–7.56 (m, 2H), 7.36–7.27 (m, 2H), 5.70 (dd, J = 10.8, 9.2 Hz, 1H), 3.76 (dd, J = 17.5, 10.9 Hz, 1H), 3.36–3.21 (m, 1H); ^{13}C NMR (75 MHz, DMSO-d_6) δ 149.1 (s, 1C), 139.9 (s, 1C), 138.5 (s, 1C), 126.3 (s, 2C), 126.2 (s, 2C), 82.9 (s, 1C), 48.4 (s, 1C). HPLC: t_r = 0.80 min, purity >95%. HRMS calcd for $C_9H_7^{79}BrNO_4S$

$[M-H]^-$ 303.9279, found 303.9281. Calcd for $C_9H_7^{79}BrNO_4S$ $[M-H]^-$ 305.9259, found 305.9260.

4-(3-Bromo-4,5-dihydroisoxazol-5-yl)benzenesulfonamide (7). Compound **7** was prepared from 4-vinylbenzenesulfonamide (**22e**, 200 mg, 1.09 mmol) following general procedure B. Purification by flash chromatography (cyclohexane/EtOAc 7:3) gave compound **7** as a white solid (256 mg, 0.84 mmol, 77% yield). R_f = 0.36 (cyclohexane/EtOAc 6:4); m.p. = 167–168 °C; ^{1}H NMR (300 MHz, DMSO-d_6) δ 7.84 (d, J = 8.4 Hz, 2H), 7.56 (d, J = 8.4 Hz, 2H), 7.40 (bs, 2H), 5.80 (dd, J = 10.9, 8.8 Hz, 1H), 3.83 (dd, J = 17.6, 11.0 Hz, 1H), 3.19 (dd, J = 8.9, 17.6 Hz, 1H); ^{13}C NMR (75 MHz, DMSO-d_6) δ 144.6 (s, 1C), 143.7 (s, 1C), 138.7 (s, 1C), 127.3 (s, 2C), 126.5 (s, 2C), 82.3 (s, 1C), 48.5 (s, 1C). HPLC: t_r = 1.20 min, purity >95%. HRMS calcd for $C_9H_9^{79}BrN_2NaO_3S$ $[M+Na]^+$ 326.9415, found 326.9409. Calcd for $C_9H_9^{81}BrN_2NaO_3S$ $[M+Na]^+$ 328.9394, found 328.9389.

5-(4-(1*H*-Tetrazol-5-yl)phenyl)-3-bromo-4,5-dihydroisoxazole (8). Compound **8** was prepared from 5-(4-vinylphenyl)-1*H*-tetrazole (**22g**, 200 mg, 1.16 mmol) following general procedure C. Recrystallization from isopropanol gave compound **8** as a white solid (208 mg, 0.71 mmol, 61% yield). R_f = 0.61 (CH_2Cl_2/methanol 95:5 + 0.5% AcOH); m.p. 195 °C dec.; ^{1}H NMR (300 MHz, DMSO-d_6) δ 8.07 (d, J = 8.5 Hz, 2H), 7.65–7.57 (m, 2H), 5.81 (dd, J = 10.9, 9.0 Hz, 1H), 3.83 (dd, J = 17.6, 10.9 Hz, 1H), 3.36 (dd, J = 17.6, 9.0 Hz, 1H); ^{13}C NMR (75 MHz, DMSO-d_6) δ 155.6 (s, 1C), 142.9 (s, 1C), 138.6 (s, 1C), 127.9 (s, 2C), 127.8 (s, 2C), 124.8 (s, 1C), 82.5 (s, 1C), 48.4 (s, 1C). HPLC: t_r = 1.53 min, purity >95%. HRMS calcd for $C_{10}H_7^{79}BrN_5O$ $[M-H]^-$ 291.9834, found 291.9831. Calcd for $C_{10}H_7^{81}BrN_5O$ $[M-H]^-$ 293.9814, found 293.9812.

3-Bromo-5-(thiophen-2-yl)-4,5-dihydroisoxazole (9). Compound **9** was prepared from 2-vinylthiophene (**25**, 200 mg, 1.82 mmol) following general procedure B. Purification by flash chromatography (cyclohexane/EtOAc 9:1) gave compound **9** as a pale-yellow oil (392 mg, 1.69 mmol, 93% yield). R_f = 0.25 (cyclohexane/EtOAc 9:1); ^{1}H NMR (300 MHz, $CDCl_3$) δ 7.35 (dd, J = 5.1, 1.3 Hz, 1H), 7.15–7.04 (m, 1H), 7.01 (dd, J = 5.0, 3.5 Hz, 1H), 5.89 (ddd, J = 10.5, 8.9, 0.7 Hz, 1H), 3.61 (dd, J = 17.3, 10.6 Hz, 1H), 3.34 (dd, J = 17.3, 9.0 Hz, 1H); ^{13}C NMR (75 MHz, $CDCl_3$) δ 141.5 (s, 1C), 136.8 (s, 1C), 127.1 (s, 1C), 126.6 (s, 1C), 126.3 (s, 1C), 79.1 (s, 1C), 49.0 (s, 1C). HPLC: t_r = 2.80 min, purity >95%. HRMS calcd for $C_7H_6^{79}BrNNaOS$ $[M+Na]^+$ 253.9251, found 253.9246. Calcd for $C_7H_6^{81}BrNNaOS$ $[M+Na]^+$ 255.9231, found 255.9226.

5-(3-Bromo-4,5-dihydroisoxazol-5-yl)thiophene-2-carboxylic acid (10). Compound **10** was prepared from 5-vinylthiophene-2-carboxylic acid (**26**, 200 mg, 1.30 mmol) following general procedure C. The crude solid product was triturated with dichloromethane and filtered under vacuum to give compound **10** as a white solid (226 mg, 0.82 mmol, 63% yield). R_f = 0.69 (cyclohexane/EtOAc 7:3 + 0.5% AcOH); m.p. 161–163 °C; ^{1}H NMR (300 MHz, DMSO-d_6) δ 13.12 (br, 1H), 7.53 (dt, J = 4.1, 2.1 Hz, 1H), 7.14 (ddt, J = 3.1, 2.1, 1.1 Hz, 1H), 6.04–5.75 (m, 1H), 3.73 (dddd, J = 17.6, 10.7, 2.7, 1.4 Hz, 1H), 3.35 (dddd, J = 17.6, 8.0, 2.7, 1.4 Hz, 1H); ^{13}C NMR (75 MHz, DMSO-d_6) δ 163.1 (s, 1C), 149.5 (s, 1C), 138.9 (s, 1C), 135.2 (s, 1C), 133.6 (s, 1C), 127.5 (s, 1C), 78.6 (s, 1C), 48.4 (s, 1C). HPLC: t_r = 1.60 min, purity >95%. HRMS calcd for $C_8H_5^{79}BrNO_3S$ $[M-H]^-$ 273.9174, found 273.9170. Calcd for $C_8H_5^{81}BrNO_3S$ $[M-H]^-$ 275.9153, found 275.9150; calcd for $C_7H_5^{79}BrNOS$ $[M-CO_2]^-$ 229.9280, found 229.9271. Calcd for $C_7H_5^{81}BrNOS$ $[M-H]^-$ 231.9260, found 231.9251.

3-Bromo-3′,4′-dihydro-2′*H*,4*H*-spiro[isoxazole-5,1′-naphthalene] (11). Prepared from 1-methylene-1,2,3,4-tetrahydronaphthalene (**29**, 200 mg, 1.39 mmol) following general procedure B. Purification by flash chromatography (cyclohexane/EtOAc 98:2) gave compound **11** as a colorless oil (265 mg, 1 mmol, 72% yield). R_f = 0.41 (cyclohexane/EtOAc 98:2); ^{1}H NMR (300 MHz, $CDCl_3$) δ 7.42–7.35 (m, 1H), 7.26–7.21 (m, 2H), 7.14–7.08 (m, 1H), 3.45 (d, J = 17.6 Hz, 1H), 3.25 (d, J = 17.6 Hz, 1H), 2.96–2.67 (m, 2H), 2.29–2.13 (m, 1H), 2.13–1.93 (m, 2H), 1.88–1.65 (m, 1H); ^{13}C NMR (75 MHz, $CDCl_3$) δ 137.5 (s, 1C), 137.2 (s, 1C), 135.1 (s, 1C), 129.0 (s, 1C), 128.3 (s, 1C), 126.9 (s, 1C), 126.6 (s, 1C), 88.0 (s, 1C), 55.4 (s, 1C), 35.9 (s, 1C), 29.0 (s, 1C), 20.2 (s, 1C). HPLC: t_r = 2.99 min, purity >95%. HRMS calcd for $C_{12}H_{12}^{79}BrNNaO$ $[M+Na]^+$ 288.0000, found 288.0004. Calcd for $C_{12}H_{12}^{81}BrNNaO$ $[M+Na]^+$ 289.9979, found 289.9984.

3-Bromo-3′,4′-dihydro-2′*H*,4*H*-spiro[isoxazole-5,1′-naphthalene]-6′-carboxylic acid (12). Prepared from 5-methylene-5,6,7,8-tetrahydronaphthalene-2-carboxylic acid (**30**, 200 mg, 1.06 mmol) following general procedure C. Purification by flash chromatography (cyclohexane/EtOAc 8:2) gave compound **12** as a white solid (239 mg, 0.77 mmol, 73% yield). R_f = 0.27 (cyclohexane/EtOAc 8:2); ^{1}H NMR (300 MHz, Methanol-d_4) δ 7.97–7.72 (m, 2H), 7.41 (d, J = 8.2 Hz, 1H), 3.43 (d, J = 3.4 Hz, 2H), 3.00–2.75 (m, 2H), 2.18–1.73 (m, 4H); ^{13}C NMR (75 MHz, Methanol-d_4) δ 168.0 (s, 1C), 142.4 (s, 1C), 137.5 (s, 1C), 135.8 (s, 1C), 130.2 (s, 1C), 130.1 (s, 1C), 127.4 (s, 1C), 126.5 (s, 1C), 87.6 (s, 1C), 54.6 (s, 1C), 35.1 (s, 1C), 28.5 (s, 1C), 19.7 (s, 1C). HPLC: t_r = 2.61 min, purity >95%. HRMS calcd for $C_{13}H_{11}^{79}BrNO_3$ $[M-H]^-$ 307.9922, found 307.9929. Calcd for $C_{13}H_{11}^{81}BrNO_3$ $[M-H]^-$ 309.9902, found 309.9908.

4.4. General bioassay procedures

4.4.1. Inhibition assays of recombinant hGAPDH

Recombinant His-tagged hGAPDH was produced in *Escherichia coli*, as already described [23]. Covalent inhibition was assayed as reported previously using a modified version of the Ferdinand assay [23]. Briefly, hGAPDH at 2 μM concentration was incubated at 25 °C or 37 °C in a buffered solution containing 10 mM TEA, 5 mM EDTA, and 10 mM sodium arseniate at pH 7.6 in the presence of the compounds at 10, 50, or 100 μM concentration. Aliquots of the reaction mixtures were sampled after 30 min, 3 h or 48 h and the residual hGAPDH activity was evaluated in a buffered solution containing 10 mM TEA, 10 mM sodium arsenate, 5 mM EDTA, 1.5 mM NAD^+ and 100 μM DL-glyceraldehyde 3-phosphate. hGAPDH was added at a final concentration of 30–50 nM, and NADH formation was monitored at 340 nm using a Cary4000 spectrophotometer (Agilent Technologies) with the cell holder thermostatted at 25 °C.

4.4.2. Spectroscopy

Absorption spectra of hGAPDH were measured using a Varian CARY400 spectrophotometer (Varian Technologies). To evaluate the disappearance of the Racker band, the protein was incubated with compounds **1**, **11**, and KA, and absorption spectra were collected until the completion of the reaction. Binding kinetics were followed at 340 nm upon incubation of 100 μM hGAPDH with 200 μM of compound **11**, KA or compound **1** in a solution containing 10 mM TEA, 5 mM EDTA, 10 mM KH_2PO_4, pH 7.6. The experimental data were fitted to the equation:

$$A_{340} = A_{340}^0 + ae^{-t/\tau} \qquad \text{Equation 1}$$

4.4.3. Molecular modeling

Molecular modeling calculations were performed on CPU/GPU hybrid High Performance Computing Cluster (10 Twin servers, for a total of 560 Intel® Xeon® Gold processors (128 GB RAM), 64 AMD® EPYC® processors and 2 GPU NVIDIA® Tesla® V100) and on High Performance Computing Cluster (6 Twin servers s for a total of 12 nodes each equipped with Intel® Xeon® QuadCore E5520 CPU, 36 GB RAM). The molecular modeling graphics were carried out on personal computer equipped with Intel(R) Core (TM) i7-8700 processor and SGI Octane 2 workstations.

The apparent pKa and logD values (pH 7.6 and 7.4) of compounds **1**–**12** were calculated by using ACD/pKa GALAS algorithm of ACD/Percepta software (ACD/Percepta, Advanced Chemistry Development, Inc., Toronto, ON, Canada, 2017, http://www.acdlabs.com). Then, the

percentage of neutral/ionized forms was computed at pH 7.6 (experimental pH value) and pH 7.4 (physiological pH value) using the Handerson−Hasselbalch equation.

Conformational analysis. The molecular models of the R and S enantiomers of **1** and **11** were built (Small Molecule tool of Discovery Studio 2017; Dassault Systèmes BIOVIA, San Diego, 2017), atomic potentials and charges were assigned using the CFF forcefield [53]. Resulting structures were subjected to molecular mechanic (MM) energy minimization ($\varepsilon = 80$*r) until the maximum RMS derivative was less than 0.001 kcal/Å, using Conjugate Gradient as minimization algorithm [54]. The obtained conformers were used as starting structures for the subsequent conformational analysis (Search Small Molecule Conformations; Discovery Studio 2017). The conformational space was sampled using the stochastic conformation search algorithm BEST for the random generation of a maximum of 200 conformations. In order to ensure a wide variance of the input structures to be fully minimized, an energy threshold value of 10^6 kcal/mol was used as selection criteria. The generated structures were then subjected to MM energy minimization (CFF forcefield; $\varepsilon = 80$*r) until the maximum RMS derivative was less than 0.001 kcal/Å, using Conjugate Gradient as minimization algorithm. The resulting conformers were ranked by their potential energy values (i.e., energy difference from the global minimum (ΔE_{GM})). The MM conformers within 5 kcal/mol from GM have been then subjected to DFT calculations. The calculations were carried out using the Gaussian 16 package [55]. All structures were fully optimized at the B3LYP/6–31+G (d,p) level [56,57] using the conductor-like polarizable continuum model (C-PCM) [35]. The C-PCM method allows the calculation of the energy in the presence of a solvent. In this case all structures were optimized as a solute in an aqueous solution. In order to characterize every structure as minimum a vibrational analysis was carried out at the same level of theory using the keyword freq. The RMS force criterion was set to 3×10^{-4} a.u. The electronic properties have been calculated using the natural bond orbital (NBO) method [58]. The resulting conformers were ranked by their potential energy and torsion angle values and compared to those obtained from MM calculations as well as to the ligand bioactive conformers obtained by docking studies.

Bioinformatics and structural analysis. Structural analysis of the selected experimentally determined structures of GAPDH were performed using the Macromolecules and Simulation tools within Discovery Studio 2017 (Dassault Systèmes BIOVIA, San Diego, 2017). The structures of the apo and holo hGAPDH (PDB IDs: 1ZNQ, 1U8F, 4WNC, 4WNI, 5C7L, 5C7O, 3PFW, 6ADE, 6YND, 6YNE, 6YNF, 6YNH) and the structures of GAPDH coming from different source organisms (listed in Table S4) in complex with the substrate (PDB IDs: 1DC4, 3KV3, 5JYA, 1NQA, 1NQO, 3CIF, 3KSZ), inhibitors (PDB IDs: 1ML3, 6QUQ, 6IQ6, 6M61, 1I32, 1I33, 1GYQ, 1IHY, 1K3T), anions (PDB IDs: 3H9E, 3GPD, 1S7C,5TSO, 7JWK), or the cations (PDB IDs: 6IO4, 7D1G) were selected and downloaded from the Protein Data Bank (PDB; http://www.rcsb.org/pdb/). All the selected structures were superimposed, and their sequence aligned according to the calculated 3D structural similarity (Cα Distance cutoff = 2.5 Å; Length Cutoff: 50; Bin Size: 20; Macromolecules tool; Discovery Studio 2017) and successively analyzed. The interactions between the protein (including co-crystallized water molecules) and the complexed ligands (NAD^+, the substrate, inhibitors, anions, and cations) were evaluated by using the nonbonded interaction criteria of the Receptor-Ligand Interaction tool (Discovery Studio 2017).

Docking studies on hGAPDH. The coordinates of the experimentally determined structure of hGAPDH were downloaded from the Brookhaven Protein DataBank (PDB ID: 1ZNQ). The coordinates of the two lacking residues at the N-terminal tail of each of the four subunits were added using the EndRepair command (Homology Module, Insight 2005). Atomic potentials and partial charges were assigned using the CFF91 force field [59] with the exception of the NAD^+ partial charges, which were assigned by MNDO semiempirical 1SCF calculation [60].

Despite the docking procedure formally requires a reasonable starting complex, it has to be underlined that the ligand conformation is fully explored during docking studies. However, the intra-cyclic torsion angles cannot be varied, thus, separate docking calculations were performed using the two almost isoenergetic conformations of the bicyclic ring of **11**. Accordingly, the lowest energy minimum conformer of **1** and the two isoenergetic lowest energy minimum conformers of **11** (considering both enantiomers for each compound) were placed in the catalytic site of hGAPDH considering the previously analyzed positioning of substrate and inhibitors (six docking runs considering both enantiomers). Starting complexes were then subjected to docking studies. A docking methodology, which considers all the systems flexible (i.e., ligand and protein), was used. Flexible docking was achieved using the Affinity module in the Insight 2005 suite, setting the SA_Docking procedure [61] and using the Cell Multipole method for non-bonded interactions [62]. The docking procedure includes a Monte Carlo (MC) based conformational search of the ligand within the active site of hGAPDH. During the first step, starting from the previously obtained roughly docked structures, the ligand was moved by a random combination of translation, rotation, and torsional changes to sample both the conformational space of the ligand and its orientation with respect to the protein (MxRChange = 3 Å; MxAngChange = 180°). During this step, van der Waals (vdW) and Coulombic terms were scaled to a factor of 0.1 to avoid very severe divergences in the vdW and Coulombic energies. If the energy of a complex structure resulting from random moves of the ligand was higher by the energy tolerance parameter than the energy of the last accepted structure, it was not accepted for minimization. To ensure a wide variance of the input structures to be successively minimized, an energy tolerance value of 10^6 kcal/mol from the previous structure was used. After the energy minimization step (conjugate gradient; 2500 iterations; $\varepsilon = 1$), the energy test, with an energy range of 50 kcal/mol, and a structure similarity check (rms tolerance = 0.3 kcal/Å) was applied to select the 20 acceptable structures. Each subsequent structure was generated from the last accepted structure.

All hGAPDH atoms were left free to move during the entire course of docking calculations, whereas, in order to avoid unrealistic results, a tethering restraint was applied the Structurally Conserved Regions (SCRs) of the protein. To identify SCRs, the hGAPDH sequence was analyzed using the Structure Prediction and Sequence Analysis server PredictProtein (http://www.predictprotein.org/). In hGAPDH, 8 α-helix and 16 β-sheet secondary structures were predicted to be highly conserved (α1, aa13−23; α2, aa40−48; α3, aa105−114; α4, aa156−166; α5, aa194−204; α6, aa211−224; α7, aa255-267; α8, aa320-332 β1, aa3-8; β2, aa28-34; β3, aa59−62; β4, aa66−70; β5, aa73−79; β6, aa93-98; β7, aa118-123; β8, aa130-135; β9, aa145-148; β10, aa170-181; β11, aa231-235; β12, aa241-249; β13, aa272-276; β14, aa293-295; β15, aa299-303; β16, aa307-314). Within the identified SCRs, the distance between backbone hydrogen bond donors and acceptors in the α-helices was restrained within 2.5 Å. On the other hand, the φ and ψ torsional angles of the β-sheets were restrained within −119° and +113°, or −139° and +135°, respectively, according to the parallel or anti-parallel structure. According to the reliability index values obtained from the secondary structure prediction analysis, we applied restraints with a quadratic form and the following set of force constants: i) 1 kcal/mol/Å^2 (maximum force: 10 kcal/mol/Å^2) for reliability index values from 0 to 3, ii) 10 kcal/mol/Å^2 (maximum force: 100 kcal/mol/Å^2) for reliability index values from 4 to 6, and iii) 100 kcal/mol/Å^2 (maximum force: 1000 kcal/mol/Å^2) for reliability index values from 7 to 9. Moreover, in order to investigate the first approach of our compounds to the catalytic site before the nucleophilic attack, a tethering restraint was applied on: i) the hydrogen bond between the catalytic residues C152 and H179 (constrained within 2.5 Å using a force constant of 100 (kcal/mol)/Å) and ii) the distance between the electrophilic carbon of BDHI ring and the sulfur atom of C152 (constrained within 3.4 Å using a force constant of 100 (kcal/mol)/Å according to the data present in the literature) [40,41]. We also performed a second MC procedure, tethering also the hydrogen bonds between NAD^+ and hGAPDH (in the substrate-free state; Table S10) within 3.4 Å (conventional hydrogen bond) or 3.8 Å

(CH–O hydrogen bond) [63,64] using a force constant of 100 (kcal/mol)/Å.

For each MC procedure, the resulting complexes were superimposed on the starting structure by fitting all the Cα atoms, and the Cα RMSD of each residue and its average value were calculated. Then, the complexes were again superimposed on the starting structure by fitting the Cα atoms of the residues characterized by an average value of RMSD ≤1.5 Å. Considering this latter superimposition, the Cα RMSD of the catalytic residues and the RMSD of NAD^+ were calculated. The χ_1 torsion angle of C152 and the geometric criteria of the hydrogen bond between C152 and H179 were also evaluated for each generated complex. In particular, the following angles of this hydrogen bond were calculated: X-D-A, D-H-A, D-A-Y, and H-A-Y angles, assuming as D the sulfur atom of C152 and as A the N_τ hydrogen atom of H179, while X is the non-hydrogen atom attached to the donor atom (i.e., C_β of C152), and Y is the atom attached to the acceptor atom (C_δ of H179).

The complexes characterized by i) Cα RMSD of C152 and H179 with respect to the starting structure ≤3 Å; ii) the *gauche(−)* conformation (from −30° to −90°) of the torsion angle χ_1 of C152 (i.e., the conformation needed to establish the hydrogen bond with H179) and iii) three out of the four angles of the hydrogen bond between C152 and H179 > 90° [65] were selected (Tables S11–S22).

The selected docked complexes were then subjected to MM energy minimization applying only the restraint on the hydrogen bond between the catalytic residues C152 and H179 (RMS derivative <0.5 kcal/Å; Steepest Descent algorithm; ε = 80*r; Module Discover; Insight 2005). The optimized complexes were again filtered by the using in addition to the above reported criteria the distance between the electrophilic carbon C3 of BDHI ring and the sulfur atom of C152 ≤ 4 Å (Table S23). The filtered complexes were analyzed and those presenting the leaving bromine atom orientated towards the anion binding sites (identified by the bioinformatics and structural analysis) or towards the NAD^+ cofactor were selected (Table S24). The non-bonded interaction energy (vdW and electrostatic energy contribution; Group Based method [66]; CUT_OFF = 100; ε = 2*r; Discover_3 Module of Insight2005) was calculated. The complexes with the most favorable interaction energy were chosen as the structures representing the most probable calculated approach of the enantiomers of **1** and **11** to the catalytic cysteine of hGAPDH. The quality of the selected docked complexes was checked using Procheck structure evaluator software [67].

4.4.4. Assessment of intrinsic warhead reactivity (kchem) using β-mercaptoethanol

The intrinsic warhead reactivity has been assessed according to Ref. [34], with some changes in the experimental procedure. Briefly, aliquots of 2 mM test compound stock solutions in MeOH were prepared. A HPLC vial (final volume = 1500 μL) was filled with (i) 750 μL of the 2 mM test compound stock solution to have a final concentration in the vial equal to 1 mM; (ii) 375 μL DMSO; (iii) 285 μL phosphate-buffered saline (PBS). The solutions were maintained at 37 °C and analyzed using an Ultimate 3000SD System from ThermoFisher with LPG-3400SD pump system, ACC-3000 autosampler and column oven, and DAD-3000 diode array detector. An Acclaim-120C18 reversed-phase column from ThermoFisher was used as stationary phase. Gradient elution (5:95 for 0.2 min, 5:95 → 100:0 over 10 min, 100:0 for 3 min) of the mobile phase consisting of ACN/MeOH:H_2O (10:90) was used at a flow rate of 0.5 mL/min at 40 °C. The pH was adjusted to 9 and 11 with aq. NaOH solution (1 M). After the first injection (time zero), 90 μL of a stock solution (10 M) of β-mercaptoethanol (βME) in PBS were added to have a final concentration in the HPLC vial equal to 600 mM. The loss of inhibitor and formation of inhibitor + βME adduct was monitored every 20 min for fast reacting compounds and every 1 h for moderate reacting molecules. The inhibitor + βME adduct was identified by MALDI-ToF mass spectra obtained on a Voyager-DeTM Pro measured in *m/z* (see Supporting Information). The percent of inhibitor + βME adduct in each sample was determined by measuring the area under the curve in HPLC chromatograms. Moles of inhibitors were plotted versus time (in seconds) using GraphPad Prism to determine *k*' for the reaction (unit of *k*' = s^{-1}). Dividing *k*' for the concentration of βME used in the assay, pseudo-first order reactions were converted into second-order reaction and k_{chem} was determined (unit of $k_{chem} = M^{-1} \bullet s^{-1}$). The experiments were performed in duplicates and standard deviations were calculated.

4.4.5. Cell cultures

Normal not-transformed fibroblasts and human pancreatic ductal adenocarcinoma (PDAC) cell lines PaCa-3, PaCa-44, PANC-1, and MIA PaCa-2 were grown in DMEM-Glutamax medium (Thermo Fisher Scientific, Milan, Italy), supplemented with 10% fetal bovine serum (FBS) and 50 μg/ml gentamicin sulfate (all from Gibco, Thermo-Fisher Scientific, Milan), and incubated at 37 °C with 5% CO_2. PaCa-3 and PaCa-44 cell lines were kindly provided by Prof. Aldo Scarpa (University of Verona, Italy) and they were obtained from patients with pancreatic ductal adenocarcinoma. All other cell lines were purchased by ATCC (Manassas, Virginia, USA). Pancreatic ductal adenocarcinoma cells were previously characterized [68]. All hGAPDH inhibitors were solubilized in DMSO (100 mM) and stored at −80 °C until use.

4.4.6. Cell proliferation assay

Cells were seeded in a 96-well plate (8×10^3 cells/well for fibroblasts and 5×10^3 cells/well for PDAC cells) and after 24 h they were treated with different concentrations (ranging from 1 μM to 100 μM) of two hGAPDH inhibitors (compounds **11** and **12**) for 48 h. At the end of the treatment, cell viability for adherent cells was measured by Crystal Violet assay according to the manufacturer's protocol [69], and absorbance (A_{595}nm) was measured by spectrophotometric analysis (GENios Pro, Tecan). Three independent experiments were performed for each assay condition.

4.4.7. Enzyme assays on cell lysates

Cells were incubated with either 10 or 100 μM compounds **11** or **12** (see above) during growth. They were then subjected to cycles of centrifugation and resuspension to remove the unreacted compounds. Finally, the cell pellets were flash-frozen. Before evaluation of GAPDH activity, cells were thawed and lysis was produced through three freeze-thaw cycles in 100 μL of a solution containing 200 mM NaCl, 1 mM EDTA, 20 mM CHAPS, 10% sucrose. The hGAPDH activity of cell lysates was measured on 10 μL of cell lysate.

Accession codes

PDB code 1ZNQ was used for docking studies of compounds (*S*)-**1**, (*R*)-**1**, (*S*)-**11** and (*R*)-**11** on hGAPDH.

Authors Contribution

The manuscript was written through contributions of all authors. All authors have given approval to the final version of the manuscript.

Declaration of competing interest

The authors declare that they have no known competing financial interests or personal relationships that could have appeared to influence the work reported in this paper.

Data availability

All experimental data are reported in Supporting Information and in the experimental section in main text

Acknowledgements

The authors acknowledge Unitech COSPECT Mass Spectrometry

Facility at the University of Milan (Italy) for the HRMS analysis. Chiara Borsari (C.B.) thanks L'Oréal Italy for Women and Science in collaboration with Italy's National Commission for UNESCO for the "L'Oréal Italia for Women in Science" fellowship. C.B. was supported by Fondazione Umberto Veronesi, Italy.

Appendix A. Supplementary data

Supplementary data to this article can be found online at https://doi.org/10.1016/j.ejmech.2023.115286.

References

[1] N.W. Seidler, GAPDH and intermediary metabolism, Adv. Exp. Med. Biol. 985 (2013) 37–59.
[2] G.S. Krasnov, A.A. Dmitriev, A.V. Snezhkina, A.V. Kudryavtseva, Deregulation of glycolysis in cancer: glyceraldehyde-3-phosphate dehydrogenase as a therapeutic target, Expert Opin. Ther. Targets 17 (2013) 681–693.
[3] S. Ganapathy-Kanniappan, Evolution of GAPDH as a druggable target of tumor glycolysis? Expert Opin. Ther. Targets 22 (2018) 295–298.
[4] S. Ganapathy-Kanniappan, R. Kunjithapatham, J.F. Geschwind, Glyceraldehyde-3-phosphate dehydrogenase: a promising target for molecular therapy in hepatocellular carcinoma, Oncotarget 3 (2012) 940–953.
[5] O. Warburg, F. Wind, E. Negelein, The metabolism of tumors in the body, J. Gen. Physiol. 8 (1927) 519–530.
[6] M.G. Vander Heiden, L.C. Cantley, C.B. Thompson, Understanding the Warburg effect: the metabolic requirements of cell proliferation, Science 324 (2009) 1029–1033.
[7] R. Pacchiana, N. Mullappilly, A. Pinto, S. Bova, S. Forciniti, G. Cullia, E. Dalla Pozza, E. Bottani, I. Decimo, I. Dando, S. Bruno, P. Conti, M. Donadelli, 3-Bromo-Isoxazoline derivatives inhibit GAPDH enzyme in PDAC cells triggering autophagy and apoptotic cell death, Cancers 14 (2022).
[8] G. Butera, N. Mullappilly, F. Masetto, M. Palmieri, M.T. Scupoli, R. Pacchiana, M. Donadelli, Regulation of autophagy by nuclear GAPDH and its Aggregates in cancer and Neurodegenerative Disorders, Int. J. Mol. Sci. 20 (2019).
[9] M.A. Sirover, Pleiotropic effects of moonlighting glyceraldehyde-3-phosphate dehydrogenase (GAPDH) in cancer progression, invasiveness, and metastases, Cancer Metastasis Rev. 37 (2018) 665–676.
[10] A. Colell, D.R. Green, J.E. Ricci, Novel roles for GAPDH in cell death and carcinogenesis, Cell Death Differ. 16 (2009) 1573–1581.
[11] J. Mohara, I. Aguilera, B.I. Goldman, C.A. Fisher, J.P. Gaughan, J.R. Libonati, S. Furukawa, A.K. Singhal, Effects of nutrient and hemoglobin enriched cell free perfusates upon ex vivo isolated rat heart preparation, ASAIO J. 51 (2005) 288–295.
[12] C.J. Martyniuk, B. Fang, J.M. Koomen, T. Gavin, L. Zhang, D.S. Barber, R. M. Lopachin, Molecular mechanism of glyceraldehyde-3-phosphate dehydrogenase inactivation by alpha,beta-unsaturated carbonyl derivatives, Chem. Res. Toxicol. 24 (2011) 2302–2311.
[13] A. Galbiati, A. Zana, P. Conti, Covalent inhibitors of GAPDH: from unspecific warheads to selective compounds, Eur. J. Med. Chem. 207 (2020), 112740.
[14] M.D. Kornberg, N. Sen, M.R. Hara, K.R. Juluri, J.V. Nguyen, A.M. Snowman, L. Law, L.D. Hester, S.H. Snyder, GAPDH mediates nitrosylation of nuclear proteins, Nat. Cell Biol. 12 (2010) 1094–1100.
[15] M.D. Kornberg, P. Bhargava, P.M. Kim, V. Putluri, A.M. Snowman, N. Putluri, P. A. Calabresi, S.H. Snyder, Dimethyl fumarate targets GAPDH and aerobic glycolysis to modulate immunity, Science 360 (2018) 449–453.
[16] M.C. Shoshan, 3-Bromopyruvate: targets and outcomes, J. Bioenerg. Biomembr. 44 (2012) 7–15.
[17] A. Endo, K. Hasumi, K. Sakai, T. Kanbe, Specific inhibition of glyceraldehyde-3-phosphate dehydrogenase by koningic acid (heptelidic acid), J. Antibiot. (Tokyo) 38 (1985) 920–925.
[18] Y. Tanaka, K. Shiomi, K. Kamei, M. Sugoh-Hagino, Y. Enomoto, F. Fang, Y. Yamaguchi, R. Masuma, C.G. Zhang, X.W. Zhang, S. Omura, Antimalarial activity of radicicol, heptelidic acid and other fungal metabolites, J. Antibiot. (Tokyo) 51 (1998) 153–160.
[19] N.J. Rahier, N. Molinier, C. Long, S.K. Deshmukh, A.S. Kate, P. Ranadive, S. A. Verekar, M. Jiotode, R.R. Lavhale, P. Tokdar, A. Balakrishnan, S. Meignan, C. Robichon, B. Gomes, Y. Aussagues, A. Samson, F. Sautel, C. Bailly, Anticancer activity of koningic acid and semisynthetic derivatives, Bioorg. Med. Chem. 23 (2015) 3712–3721.
[20] C. Jing, Y. Li, Z. Gao, R. Wang, Antitumor activity of Koningic acid in thyroid cancer by inhibiting cellular glycolysis, Endocrine 75 (2022) 169–177.
[21] D.E. Cane, J.K. Sohng, Inhibition of glyceraldehyde-3-phosphate dehydrogenase by pentalenolactone: kinetic and mechanistic studies, Arch. Biochem. Biophys. 270 (1989) 50–61.
[22] G. Cullia, S. Bruno, S. Parapini, M. Margiotta, L. Tamborini, A. Pinto, A. Galbiati, A. Mozzarelli, M. Persico, A. Paladino, C. Fattorusso, D. Taramelli, P. Conti, Covalent inhibitors of Plasmodium falciparum glyceraldehyde 3-phosphate dehydrogenase with antimalarial activity in vitro, ACS Med. Chem. Lett. 10 (2019) 590–595.
[23] S. Bruno, M. Margiotta, A. Pinto, G. Cullia, P. Conti, C. De Micheli, A. Mozzarelli, Selectivity of 3-bromo-isoxazoline inhibitors between human and Plasmodium falciparum glyceraldehyde-3-phosphate dehydrogenases, Bioorg. Med. Chem. 24 (2016) 2654–2659.
[24] S. Bruno, A. Pinto, G. Paredi, L. Tamborini, C. De Micheli, V. La Pietra, L. Marinelli, E. Novellino, P. Conti, A. Mozzarelli, Discovery of covalent inhibitors of glyceraldehyde-3-phosphate dehydrogenase, a target for the treatment of malaria, J. Med. Chem. 57 (2014) 7465–7471.
[25] C. Ballatore, D.M. Huryn, A.B. Smith 3rd, Carboxylic acid (bio)isosteres in drug design, ChemMedChem 8 (2013) 385–395.
[26] C.D. Siebert, Das Bioisosterie-Konzept: Arzneistoffentwicklung, Chem. Unserer Zeit 38 (2004) 320–324.
[27] Z. Fang, Y. Song, P. Zhan, Q. Zhang, X. Liu, Conformational restriction: an effective tactic in 'follow-on'-based drug discovery, Future Med. Chem. 6 (2014) 885–901.
[28] P. Conti, C. Dallanoce, M. De Amici, C. De Micheli, R. Fruttero, Synthesis of new bicyclic analogues of glutamic acid, Tetrahedron 55 (1999) 5623–5634.
[29] A. Zana, A. Galbiati, Synthesis and reactivity of 3-Halo-4,5-dihydroisoxazoles: an overview, ChemistrySelect 6 (2021) 8249–8261.
[30] R. Kitz, I.B. Wilson, Esters of Methanesulfonic acid as irreversible inhibitors of Acetylcholinesterase, J. Biol. Chem. 237 (1962) 3245–3249.
[31] E. Racker, I. Krimsky, Mechanism of action of glyceraldehyde-3-phosphate dehydrogenase, Nature 169 (1952) 1043–1045.
[32] S. Moniot, S. Bruno, C. Vonrhein, C. Didierjean, S. Boschi-Muller, M. Vas, G. Bricogne, G. Branlant, A. Mozzarelli, C. Corbier, Trapping of the thioacylglyceraldehyde-3-phosphate dehydrogenase intermediate from Bacillus stearothermophilus. Direct evidence for a flip-flop mechanism, J. Biol. Chem. 283 (2008) 21693–21702.
[33] D. Montero, C. Tachibana, J. Rahr Winther, C. Appenzeller-Herzog, Intracellular glutathione pools are heterogeneously concentrated, Redox Biol. 1 (2013) 508–513.
[34] C. Borsari, E. Keles, J.A. McPhail, A. Schaefer, R. Sriramaratnam, W. Goch, T. Schaefer, M. De Pascale, W. Bal, M. Gstaiger, J.E. Burke, M.P. Wymann, J. Am. Chem. Soc. 144 (2022) 6326–6342.
[35] M. Cossi, N. Rega, G. Scalmani, V. Barone, Energies, structures, and electronic properties of molecules in solution with the C-PCM solvation model, J. Comput. Chem. 24 (2003) 669–681.
[36] W.J. Cook, O. Senkovich, D. Chattopadhyay, An unexpected phosphate binding site in glyceraldehyde 3-phosphate dehydrogenase: crystal structures of apo, holo and ternary complex of Cryptosporidium parvum enzyme, BMC Struct. Biol. 9 (2009) 9.
[37] C. Didierjean, C. Corbier, M. Fatih, F. Favier, S. Boschi-Muller, G. Branlant, A. Aubry, Crystal structure of two ternary complexes of phosphorylating glyceraldehyde-3-phosphate dehydrogenase from Bacillus stearothermophilus with NAD and D-glyceraldehyde 3-phosphate, J. Biol. Chem. 278 (2003) 12968–12976.
[38] M. Yun, C.G. Park, J.Y. Kim, H.W. Park, Structural analysis of glyceraldehyde 3-phosphate dehydrogenase from Escherichia coli: direct evidence of substrate binding and cofactor-induced conformational changes, Biochemistry 39 (2000) 10702–10710.
[39] M.S. Castilho, F. Pavao, G. Oliva, S. Ladame, M. Willson, J. Perie, Evidence for the two phosphate binding sites of an analogue of the thioacyl intermediate for the Trypanosoma cruzi glyceraldehyde-3-phosphate dehydrogenase-catalyzed reaction, from its crystal structure, Biochemistry 42 (2003) 7143–7151.
[40] A. Lodola, D. Branduardi, M. De Vivo, L. Capoferri, M. Mor, D. Piomelli, A. Cavalli, A catalytic mechanism for cysteine N-terminal nucleophile hydrolases, as revealed by free energy simulations, PLoS One 7 (2012), e32397.
[41] K. Arafet, S. Ferrer, F.V. Gonzalez, V. Moliner, Quantum mechanics/molecular mechanics studies of the mechanism of cysteine protease inhibition by peptidyl-2,3-epoxyketones, Phys. Chem. Chem. Phys. 19 (2017) 12740–12748.
[42] S.A. Ismail, H.W. Park, Structural analysis of human liver glyceraldehyde-3-phosphate dehydrogenase, Acta Crystallogr D Biol Crystallogr 61 (2005) 1508–1513.
[43] J.B. Park, H. Park, J. Son, S.J. Ha, H.S. Cho, Structural study of monomethyl fumarate-bound human GAPDH, Mol Cells 42 (2019) 597–603.
[44] A. Chaikuad, N. Shafqat, R. Al-Mokhtar, G. Cameron, A.R. Clarke, R.L. Brady, U. Oppermann, J. Frayne, W.W. Yue, Structure and kinetic characterization of human sperm-specific glyceraldehyde-3-phosphate dehydrogenase, GAPDS, Biochem. J. 435 (2011) 401–409.
[45] S. Mukherjee, D. Dutta, B. Saha, A.K. Das, Crystal structure of glyceraldehyde-3-phosphate dehydrogenase 1 from methicillin-resistant Staphylococcus aureus MRSA252 provides novel insights into substrate binding and catalytic mechanism, J. Mol. Biol. 401 (2010) 949–968.
[46] M.A. Robien, J. Bosch, F.S. Buckner, W.C. Van Voorhis, E.A. Worthey, P. Myler, C. Mehlin, E.E. Boni, O. Kalyuzhniy, L. Anderson, A. Lauricella, S. Gulde, J.R. Luft, G. DeTitta, J.M. Caruthers, K.O. Hodgson, M. Soltis, F. Zucker, C.L. Verlinde, E. A. Merritt, L.W. Schoenfeld, W.G. Hol, Crystal structure of glyceraldehyde-3-phosphate dehydrogenase from Plasmodium falciparum at 2.25 A resolution reveals intriguing extra electron density in the active site, Proteins 62 (2006) 570–577.
[47] G. Butera, R. Pacchiana, N. Mullappilly, M. Margiotta, S. Bruno, P. Conti, C. Riganti, M. Donadelli, Mutant p53 prevents GAPDH nuclear translocation in pancreatic cancer cells favoring glycolysis and 2-deoxyglucose sensitivity, Biochim. Biophys. Acta Mol. Cell Res. 1865 (2018) 1914–1923.
[48] H. Harami-Papp, L.S. Pongor, G. Munkacsy, G. Horvath, A.M. Nagy, A. Ambrus, P. Hauser, A. Szabo, L. Tretter, B. Gyorffy, TP53 mutation hits energy metabolism and increases glycolysis in breast cancer, Oncotarget 7 (2016) 67183–67195.
[49] C. Fiorini, M. Cordani, C. Padroni, G. Blandino, S. Di Agostino, M. Donadelli, Mutant p53 stimulates chemoresistance of pancreatic adenocarcinoma cells to gemcitabine, Biochim. Biophys. Acta 1853 (2015) 89–100.

[50] Y. Liu, W. Gu, The Complexity of P53-mediated metabolic regulation in tumor suppression, Semin. Cancer Biol. (2021).
[51] D.M. Vyas, Y. Chiang, T.W. Doyle, A short, efficient total synthesis of (±) acivicin and (±) bromo-acivicin, Tetrahedron Lett. 25 (1984) 487–490.
[52] H. Seo, A. Liu, T.F. Jamison, Direct β-selective hydrocarboxylation of Styrenes with CO(2) enabled by continuous flow Photoredox catalysis, J. Am. Chem. Soc. 139 (2017) 13969–13972.
[53] C.S. Ewig, R. Berry, U. Dinur, J.R. Hill, M.J. Hwang, H. Li, C. Liang, J. Maple, Z. Peng, T.P. Stockfisch, T.S. Thacher, L. Yan, X. Ni, A.T. Hagler, Derivation of class II force fields. VIII. Derivation of a general quantum mechanical force field for organic compounds, J. Comput. Chem. 22 (2001) 1782–1800.
[54] R. Fletcher, Unconstrained optimization, in: Practical Methods of Optimization, John Wiley & Sons Ltd, New York, NY, USA, 1980, pp. 1–128.
[55] M.J. Frisch, G.W. Trucks, H.B. Schlegel, G.E. Scuseria, M.A. Robb, J.R. Cheeseman, G. Scalmani, V. Barone, G.A. Petersson, H. Nakatsuji, X. Li, M. Caricato, A. V. Marenich, J. Bloino, B.G. Janesko, R. Gomperts, B. Mennucci, H.P. Hratchian, J. V. Ortiz, A.F. Izmaylov, J.L. Sonnenberg, Williams, F. Ding, F. Lipparini, F. Egidi, J. Goings, B. Peng, A. Petrone, T. Henderson, D. Ranasinghe, V.G. Zakrzewski, J. Gao, N. Rega, G. Zheng, W. Liang, M. Hada, M. Ehara, K. Toyota, R. Fukuda, J. Hasegawa, M. Ishida, T. Nakajima, Y. Honda, O. Kitao, H. Nakai, T. Vreven, K. Throssell, J.A. Montgomery Jr., J.E. Peralta, F. Ogliaro, M.J. Bearpark, J. J. Heyd, E.N. Brothers, K.N. Kudin, V.N. Staroverov, T.A. Keith, R. Kobayashi, J. Normand, K. Raghavachari, A.P. Rendell, J.C. Burant, S.S. Iyengar, J. Tomasi, M. Cossi, J.M. Millam, M. Klene, C. Adamo, R. Cammi, J.W. Ochterski, R.L. Martin, K. Morokuma, O. Farkas, J.B. Foresman, D.J. Fox, Gaussian 16, Rev. C.01, Wallingford, CT, 2016.
[56] A.D. Becke, Density-functional thermochemistry. III. The role of exact exchange, J. Chem. Phys. 98 (1993) 5648–5652.
[57] C. Lee, W. Yang, R.G. Parr, Development of the Colle-Salvetti correlation-energy formula into a functional of the electron density, Phys. Rev. B 37 (1988) 785–789.
[58] A.E. Reed, R.B. Weinstock, F. Weinhold, Natural population analysis, J. Chem. Phys. 83 (1985) 735–746.
[59] J.R. Maple, M.J. Hwang, T.P. Stockfisch, U. Dinur, M. Waldman, C.S. Ewig, A. T. Hagler, Derivation of class II force fields. I. Methodology and quantum force field for the alkyl functional group and alkane molecules, J. Comput. Chem. 15 (1994).
[60] M.J.S. Dewar, W. Thiel, Ground states of molecules. 38. The MNDO method. Approximations and parameters, J. Am. Chem. Soc. 99 (1977) 4899–4907.
[61] H. Senderowitz, F. Guarnieri, W.C. Still, A smart Monte Carlo Technique for free energy simulations of Multiconformational molecules. Direct calculations of the conformational Populations of organic molecules, J. Am. Chem. Soc. 117 (1995) 8211–8219.
[62] H.Q. Ding, N. Karasawa, W. A G III, Atomic level simulations on a million particles: the cell multipole method for Coulomb and London nonbond interactions, J. Chem. Phys. 97 (1992) 4309–4315.
[63] A.C. Pierce, K.L. Sandretto, G.W. Bemis, Kinase inhibitors and the case for CH...O hydrogen bonds in protein-ligand binding, Proteins 49 (2002) 567–576.
[64] D.B. McConnell, Biotin's Lessons in drug design, J. Med. Chem. 64 (2021) 16319–16327.
[65] E.N. Baker, R.E. Hubbard, Hydrogen bonding in globular proteins, Prog. Biophys. Mol. Biol. 44 (1984) 97–179.
[66] P.J. Steinbach, B.R. Brooks, New spherical-cutoff methods for long-range forces in macromolecular simulation, J. Comput. Chem. 15 (1994) 667–683.
[67] R.A. Laskowski, M.W. MacArthur, D.S. Moss, J.M. Thornton, PROCHECK: a program to check the stereochemical quality of protein structures, J. Appl. Crystallogr. 26 (1993) 283–291.
[68] P.S. Moore, B. Sipos, S. Orlandini, C. Sorio, F.X. Real, N.R. Lemoine, T. Gress, C. Bassi, G. Kloppel, H. Kalthoff, H. Ungefroren, M. Lohr, A. Scarpa, Genetic profile of 22 pancreatic carcinoma cell lines. Analysis of K-ras, p53, p16 and DPC4/Smad4, Virchows Arch. 439 (2001) 798–802.
[69] M. Feoktistova, P. Geserick, M. Leverkus, Crystal violet assay for determining viability of cultured cells, Cold Spring Harb. Protoc. 2016 (2016) pdb prot087379.